JCI The Journal of Clinical Investigation

Oncogenic KRAS signaling drives evasion of innate immune surveillance in lung adenocarcinoma by activating CD47

Huanhuan Hu, … , Chao Yan, Xi Chen

J Clin Invest. 2022. https://doi.org/10.1172/JCI153470.

Research In-Press Preview Oncology Pulmonology

Graphical abstract

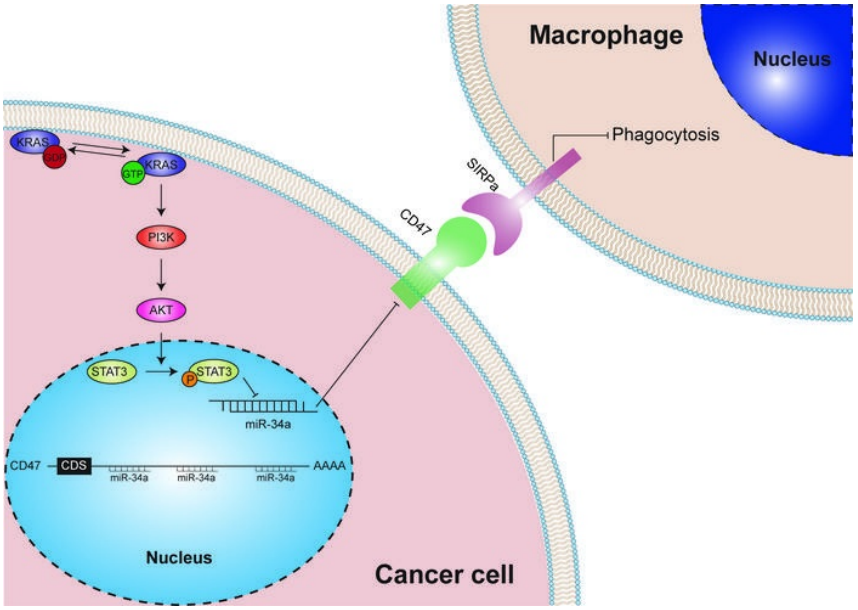

Oncogenic KRAS signaling drives evasion of innate immune surveillance in lung adenocarcinoma by activating CD47

Huanhuan Hu[1,2,†], Rongjie Cheng[1,3,†], Yanbo Wang[1,2†], Xiaojun Wang[4†], Jianzhuang Wu[1], Yan Kong[1], Shoubin Zhan[1], Zhen Zhou[1], Hongyu Zhu[1], Ranran Yu[1], Gaoli Liang[1], Qingyan Wang[1], Xiaoju Zhu[1], Chen-Yu Zhang[1,5,8], Rong Yin[4,6,7,*], Chao Yan[1,2,8,*], Xi Chen[1,2,5,8,9,*]

Affiliations:

[1]State Key Laboratory of Pharmaceutical Biotechnology, Jiangsu Engineering Research Center for MicroRNA Biology and Biotechnology, NJU Advanced Institute of Life Sciences (NAILS), School of Life Sciences, Nanjing University; Nanjing 210023, China.

[2]Chemistry and Biomedicine Innovation Center (ChemBIC), Nanjing University; Nanjing 210023, China.

[3]Cancer Stem Cell Laboratory, The Breast Cancer Now Toby Robins Research Centre, The Institute of Cancer Research; London, SW3 6JB, UK.

[4]Department of Thoracic Surgery, Jiangsu Key Laboratory of Molecular and Translational Cancer Research, Jiangsu Cancer Hospital & Nanjing Medical University Affiliated Cancer Hospital & Jiangsu Institute of Cancer Research; Nanjing 210009, China.

[5]Research Unit of Extracellular RNA, Chinese Academy of Medical Sciences, Nanjing, Jiangsu 210023, China.

[6]Biobank of Lung Cancer, Jiangsu Biobank of Clinical Resources; Nanjing 210009, China.

[7]Collaborative Innovation Centre for Cancer Personalized Medicine, Nanjing Medical University; Nanjing 210009, China.

[8]Institute of Artificial Intelligence Biomedicine, Nanjing University; Nanjing 210023, China.

[9]Pingshan Translational Medicine Center, Shenzhen Bay Laboratory, Shenzhen, Guangdong 518055, China.

[*]Address correspondence to: Xi Chen, Nanjing University School of Life Sciences, 163 Xianlin Avenue, Nanjing, 210023, China; Phone: 86-25-89681276; Email: xichen@nju.edu.cn. Chao Yan, Nanjing University School of Life Sciences, 163 Xianlin Avenue, Nanjing, 210023, China; Phone: 86-25-89681662; Email: yanchao@nju.edu.cn. Rong Yin, Department of Thoracic Surgery, Jiangsu Cancer Hospital, 42 Baiziting, Nanjing, 210009, China; Phone: 86-25-83283480; Email: rong_yin@njmu.edu.cn.

[†]These authors contributed equally to this work.

COI statement: The authors have declared that no conflict of interest exists.

ABSTRACT

KRAS is one of the most frequently activated oncogenes in human cancers. While the role of *KRAS* mutation in tumorigenesis and tumor maintenance has been extensively studied, the relationship between KRAS and the tumor immune microenvironment is not fully understood. Herein, we identified a novel role of KRAS in driving tumor evasion from innate immune surveillance. In lung adenocarcinoma patient samples and *Kras*-driven genetic mouse models of lung cancer, mutant KRAS activated the expression of cluster of differentiation 47 (CD47), an antiphagocytic signal in cancer cells, leading to decreased phagocytosis of cancer cells by macrophages. Mechanistically, mutant KRAS activated PI3K-STAT3 signaling, which restrained miR-34a expression and relieved the post-transcriptional repression of miR-34a on CD47. In three independent lung cancer patient cohorts, *KRAS* mutation status positively correlated with CD47 expression. Therapeutically, disruption of the KRAS-CD47 signaling axis with *KRAS* siRNA, the $KRAS^{G12C}$ inhibitor AMG 510 or miR-34a mimic suppressed CD47 expression, enhanced the phagocytic capacity of macrophages and restored innate immune surveillance. Our results revealed a direct mechanistic link between active KRAS and innate immune evasion and identified CD47 as a major effector underlying KRAS-mediated immunosuppressive tumor microenvironment.

INTRODUCTION

Mutations in the *KRAS* gene are the most common drivers of tumor development across a spectrum of human cancers, such as cancers of the lung, colon, and pancreas (1-3). For example, around 30% of lung adenocarcinomas harbor *KRAS* mutations, with $KRAS^{G12C}$ being the most common subtype (12-15%) (4). At the molecular level, KRAS proteins with activating mutations abrogate the GTPase activity and are locked in the GTP-bound hyperactive state, leading to constitutive activation of downstream pro-proliferative and pro-survival pathways such as RAF-MEK-ERK and PI3K-AKT (5, 6). Despite forty years of intensive efforts to develop targeted therapy for the KRAS oncoprotein, AMG 510, a covalent inhibitor of the $KRAS^{G12C}$ mutation, has just been approved by the FDA in May 2021; and targeting other KRAS mutations is still considered “mission impossible” (7, 8). Understanding how KRAS mutations drive cancer pathogenesis and developing new intervention strategies are the major priorities for conquering *KRAS*-driven cancers.

An emerging and exciting new direction may come from recent advances in our understanding of the relationship between KRAS mutations and tumor immune evasion. Tumor cells often overexpress immune checkpoint molecules to escape immune surveillance. As two representative checkpoint molecules often overexpressed on the surface of cancer cells, programmed death-ligand 1 (PD-L1) signals to T cells to evade attacks from the adaptive immune system, whereas cluster of differentiation 47 (CD47) is a critical anti-phagocytosis signal to macrophages in the innate immune system (9-11). Recently, Coelho et al. unveiled a novel function of oncogenic KRAS signaling (mainly the $KRAS^{G12V}$ mutation) in driving tumor cell PD-L1 expression, thereby impairing adaptive immune surveillance and favoring tumor

growth (12). Canon et al. also showed that the $KRAS^{G12C}$ inhibitor AMG 510 could drive antitumor immunity through inhibiting PD-L1 signaling (13). While KRAS-mediated evasion of the adaptive immune response has been increasingly recognized, whether KRAS plays a role in innate immune surveillance has not been delineated.

The innate immune system plays an important role in tumor surveillance mainly through the phagocytic activity of macrophages. In the early stage of tumor formation, macrophages actively infiltrate tumor tissues and phagocytose tumor cells; later on, their phagocytic capacity are gradually suppressed by tumor-derived inhibitory signals (14). As the most studied anti-phagocytosis signal in the tumor microenvironment, CD47 has been shown to be overexpressed on the surface of many types of cancer cells. Binding of CD47 to its receptor signal regulatory protein α (SIRPα) on macrophages inhibits macrophage-mediated phagocytosis (15). High CD47 expression in the tumor microenvironment has also been associated with poor patient prognosis in various cancer types (16-19). Moreover, therapeutic blockade of the CD47-SIRPα axis using anti-CD47 monoclonal antibodies has demonstrated efficacy in a variety of preclinical models and is currently in clinical trials for both leukemia and solid tumors (20). However, little is known about the genetic and epigenetic regulation of the expression of CD47 in cancer cells.

In this study, we showed that oncogenic KRAS mutations interact with the innate immune system in the context of lung adenocarcinoma progression by promoting tumor cell evasion from macrophage phagocytosis. We also dissected the underlying molecular mechanisms and revealed that KRAS mutations could directly activate CD47 in cancer cells to inhibit the activity of macrophages, thereby leading to innate immune evasion and aggressive tumor progression. We

therefore propose that *KRAS* mutation status could serve as a biomarker for anti-CD47 cancer immunotherapy.

RESULTS

KRAS mutations render lung cancer cells insensitive to phagocytosis by macrophages

We set out to investigate whether *KRAS* mutations could lead to impaired innate immune response against tumors in 18 lung adenocarcinoma patients (12 were *KRAS* wild-type ($KRAS^{WT}$) and 6 harbored the $KRAS^{G12C}$ mutation). Primary tumor cells freshly isolated from surgically-removed tumor tissues were fluorescently labeled with CFSE and cocultured with human peripheral blood monocyte-derived macrophages and analyzed by fluorescence-activated cell sorting (FACS) to quantify cancer cells that were phagocytosed by macrophages. Tumors cells derived from patients with *KRAS* mutation showed significantly less phagocytosis by macrophages (Figure 1A and Supplementary Figure 1A). A similar phagocytosis assay was carried out using the human lung cancer cell line H358 harboring $KRAS^{G12C}$ mutation. CFSE-labeled H358 cells were cocultured with human peripheral blood monocyte-derived macrophages and analyzed by FACS or fluorescence microscopy; overexpression of $KRAS^{G12C}$, but not $KRAS^{WT}$, led to decreased phagocytosis of H358 cells by macrophages, whereas siRNA knockdown of *KRAS* increased phagocytosis (Figure 1B and Supplementary Figure 1B-F). We also established a lung colonization model by tail vein injection of eGFP-labeled H358 cells into nude mice (Figure 1C). The infiltration of macrophages in mouse lung tumors was analyzed by immunofluorescence staining with antibodies against the typical myeloid marker CD11b and the tumoricidal M1 macrophage marker iNOS. Although the M1 macrophage population ($CD11b^+iNOS^+$ or $iNOS^+TNF\text{-}\alpha^+$ by immunohistochemistry) was continuously present in the tumor tissue over the 3-month experiment period (Figure 1D and Supplementary Figure 2A), the co-localization of the CD11b/iNOS signal and the eGFP signal displayed a gradual decrease over time (Figure 1D), indicating impaired macrophage phagocytosis of H358 tumor cells in vivo.

We further confirmed this observation in two *Kras*-driven genetically engineered mouse models of lung cancer, the Lox-Stop-Lox-*Kras*^{G12D} (*Kras*$^{LSL\text{-}G12D/+}$) mouse strain and the *Kras*$^{LSL\text{-}G12D/+}$;*p53*$^{fl/fl}$ mouse strain (21, 22). The *Kras*$^{LSL\text{-}G12D/+}$ mice developed spontaneous, sporadic pulmonary adenocarcinomas following intratracheal administration of the Cre-expressing adenovirus (Adeno-Cre) to remove the Stop element from the *Kras*^{G12D} allele; while the *Kras*$^{LSL\text{-}G12D/+}$;*p53*$^{fl/fl}$ mice exhibited accelerated pulmonary adenocarcinoma formation by the concomitant deletion of the *Tp53* tumor suppressor gene. As expected, spontaneous formation of small adenocarcinomas was observed in the lungs of the *Kras*$^{LSL\text{-}G12D/+}$ mice 5 months after Adeno-Cre administration (Supplementary Figure 2B, C), whereas pulmonary adenocarcinomas were present in the *Kras*$^{LSL\text{-}G12D/+}$;*p53*$^{fl/fl}$ mice at 1 month and substantially increased at 3 months (Figure 1E and Supplementary Figure 3A, B). We then analyzed the status of macrophage infiltration and tumor phagocytosis in the lung tumors from both the *Kras*$^{LSL\text{-}G12D/+}$ and *Kras*$^{LSL\text{-}G12D/+}$;*p53*$^{fl/fl}$ mice. Similar to the H358 model, a gradual decrease in macrophage phagocytosis of tumor cells was observed over time (Figure 1F and Supplementary Figure 2D) despite the continuous presence of M1 macrophages, which was confirmed by immunohistochemistry (IHC) with the M1 macrophage markers iNOS and TNF-α (Supplementary Figure 2E and 3C). Together, these results suggested that *KRAS* mutations endowed lung cancer cells with antiphagocytic capacity during tumor progression.

CD47 is required for KRAS-driven antiphagocytic effect in lung cancer

Since cell-surface expression of CD47 is a major mechanism used by cancer cells to evade macrophage phagocytosis, we investigated whether *KRAS* mutation status could affect CD47

expression in lung tumors. We first analyzed CD47 expression on the surface of tumor cells isolated from the 18 paired lung adenocarcinoma patient samples by flow cytometry. Patients with *KRAS* mutations displayed a higher level of CD47 expression on tumor cell surface (Figure 2A and Supplementary Figure 4A). Next, in both the $Kas^{LSL\text{-}G12D/+}$ and $Kras^{LSL\text{-}G12D/+};p53^{fl/fl}$ mice, CD47 protein expression in the lung also gradually increased over time (Figure 2B, C and Supplementary Figure 4B-E). We then used the *Ras*-less mouse embryonic fibroblast (MEF) model (23) to investigate the role of *Kras* mutations in regulating CD47 expression. CD47 protein levels were significantly elevated in the *Ras*-less MEFs stably overexpressing $KRAS^{G12C}$ or $KRAS^{G12D}$ compared with $KRAS^{WT}$ (Figure 2D and Supplementary Figure 5A). Moreover, we used two human lung cancer cell lines, H358 ($KRAS^{G12C}$) and SK-LU-1 ($KRAS^{G12D}$), to further illustrate the potential regulation of CD47 by KRAS. Overexpression of the respective $KRAS^{MUT}$, but not $KRAS^{WT}$, led to significant induction of CD47 expression in H358 and SK-LU-1 cells (Figure 2E and Supplementary Figure 5B, C). In contrast, siRNA knockdown of *KRAS* significantly decreased CD47 expression in both cell lines (Figure 2F and Supplementary Figure 5D, E). These data indicated that *KRAS* mutations could drive CD47 expression both in vitro and in vivo.

To investigate whether CD47 is required for *KRAS*-driven tumor evasion from macrophage phagocytosis, we treated the $Kras^{LSL\text{-}G12D/+};p53^{fl/fl}$ mice with *Cd47* shRNA delivered by adeno-associated virus (AAV) along with intratracheal administration of Adeno-Cre. Knockdown of *Cd47* significantly decreased tumor formation in the lungs of mice and prolonged overall survival (Figure 2G-K and Supplementary Figure 6A-D). Importantly, *Cd47* knockdown also substantially increased the infiltration of M1 macrophages in tumor tissues and the phagocytosis

of tumor cells by M1 macrophages in vivo (Figure 2L and Supplementary Figure 6E). Taken together, these data suggested that CD47 wass involved in *KRAS*-driven tumor progression by restraining the antitumorigenic properties of macrophages.

MiR-34a is a negative regulator of CD47-mediated antiphagocytic activity

While our data showed a positive correlation between *KRAS* mutation status and CD47 protein levels in both mice and human tumors, *CD47* mRNA levels were unaffected by *KRAS* mutation status (Supplementary Figure 7), suggesting the involvement of post-transcriptional regulatory mechanisms. Since miRNAs represent a fundamental and common post-transcriptional regulator of gene expression (24), we hypothesized that KRAS may regulate CD47 expression through miRNAs. We therefore employed small RNA deep sequencing to determine the alteration of miRNA profiles in the lung tumors from $Kras^{LSL\text{-}G12D/+}$ mice compared with the normal lung tissues from mice without Adeno-Cre treatment. By applying a stringent threshold of $\log_2$ (fold-change) > 1 and significance criterion of $p < 0.05$, a total of 10 miRNAs were found to be significantly increased in the lung tumors, while 40 miRNAs exhibited a decreasing trend (Figure 3A). Hierarchical clustering also revealed the separation of the tumorous from normal tissues based on miRNA profiling (Figure 3B). Subsequently, the expression of some top-ranked dysregulated miRNAs (mean reads > 500, $\log_2$ fold-change > 1 and $p < 0.01$) (Supplementary Table 1) was confirmed by quantitative RT-PCR; 7 of the 9 miRNAs were differentially expressed in the lung tumors compared with the normal tissues (Figure 3C). Because miRNAs usually suppress the expression of their target genes, we focused on the five miRNAs that were decreased during tumorigenesis. Using three different computational software programs (TargetScan, miRanda, and PicTar), we identified miR-34a-5p (miR-34a), one of the five most

downregulated miRNAs in the lung tumors of the *Kras*$^{LSL\text{-}G12D/+}$ mice, as a potential regulator of CD47 expression. A total of three specific miR-34a binding sites were identified in the 3'-untranslated region (3'-UTR) of CD47 (Supplementary Figure 8A).

To further validate the correlation between miR-34a and CD47, we assessed the CD47 protein levels in H358 and SK-LU-1 cells after transfection with miR-34a mimic (synthetic double-stranded RNA oligonucleotide that mimics the precursor of miR-34a) or with miR-34a antisense (single-stranded, chemically modified oligonucleotide designed to specifically bind to and inhibit mature miR-34a) (Supplementary Figure 8B, C). The CD47 protein levels were significantly suppressed by miR-34a mimic and increased by miR-34a antisense in both H358 and SK-LU-1 cells (Figure 3D, E and Supplementary Figure 8D-G), whereas the *CD47* mRNA levels were not affected (Supplementary Figure 8H, I). Furthermore, direct binding of miR-34a to the 3'-UTR of *CD47* mRNA was also confirmed in a luciferase reporter assay (Supplementary Figure 8J). On the contrary, the other four miRNAs that were downregulated in tumor tissues did not affect CD47 expression in the same assay (Supplementary Figure 9). These results demonstrated that miR-34a could directly bind to the 3'-UTR of *CD47* mRNA and inhibit CD47 translation. Next, we evaluated the effect of miR-34a on the antiphagocytic activity of CD47 in lung cancer. Introduction of the miR-34a mimic into H358 cells significantly promoted macrophage-mediated phagocytosis, which was reversed by co-transfection with the CD47 overexpression plasmid (Figure 3F and Supplementary Figure 10A, B).

Subsequently, we evaluated the in vivo effects of miR-34a on *KRAS*-driven tumorigenesis and macrophage infiltration. AAV-mediated delivery of miR-34a at the time of intratracheal Adeno-

Cre administration in the *Kras*$^{LSL\text{-}G12D/+}$;*p53*$^{fl/fl}$ mice significantly decreased lung tumor formation and prolonged overall survival, which could be completely rescued by coadministration of AAV-mediated CD47 overexpression plasmid (Figure 4A-C and Supplementary Figure 10C, D). Similar to *Cd47* knockdown (Figure 2J-L), miR-34a overexpression strongly inhibited CD47 protein levels and promoted tumor phagocytosis by M1 macrophages; co-treatment with AAV-CD47 in mice completely reversed the effect of miR-34a (Figure 4D-G and Supplementary Figure 10E-G). These results indicated that the escape from innate immune surveillance induced by CD47 was controlled, at least in part, by miR-34a.

The PI3K-STAT3 axis mediates KRAS-driven miR-34a suppression and CD47 activation

To illustrate how miR-34a connects oncogenic KRAS signaling to CD47 expression, we first determined the relationship between *KRAS* mutation/expression and miR-34a expression. In *Ras*-less MEFs, overexpression of KRAS^{G12C} or KRAS^{G12D} decreased miR-34a levels compared with overexpression of KRAS^{WT} (Figure 5A). Similarly, overexpression of KRAS^{G12C} or KRAS^{G12D} but not KRAS^{WT} decreased miR-34a levels in H358 and SK-LU-1 cells (Figure 5B, D). In contrast, KRAS knockdown resulted in an increase in miR-34a expression in both cell lines (Figure 5C, E). A gradual decrease in the miR-34a level was also observed in both the *KRAS*$^{LSL\text{-}G12D/+}$ and *KRAS*$^{LSL\text{-}G12D/+}$;*p53*$^{fl/fl}$ mice upon activation of the oncogenic activity of KRAS^{G12D} (Figure 5F, G). These data indicated that oncogenic *KRAS* mutations functioned as a negative regulator of miR-34a expression during *KRAS*-driven lung tumorigenesis.

To determine which signaling pathway downstream of KRAS is responsible for regulating miR-34a expression, we blocked the RAF-MEK-ERK pathway with a MEK inhibitor (GSK1120212, trametinib) and the PI3K-AKT pathway with a PI3K inhibitor (GDC-0941, pictilisib), respectively, in MEFs and H358 cells. While the MEK inhibitor had no effect on the expression of miR-34a and CD47; the PI3K inhibitor, either alone or in combination with the MEK inhibitor, substantially induced miR-34a expression (Figure 5H) and decreased CD47 levels (Figure 6A and Supplementary Figure 11A) in both MEFs and H358 cells. These results revealed a direct mechanistic link between the PI3K pathway and miR-34a expression in lung cancer cells.

Recent studies have uncovered an interdependence of PI3K and STAT3 signaling in cancer cells (25, 26); in particular, STAT3 was phosphorylated at Tyr705 and activated in a PI3K-dependent manner. Because STAT3 is a well-known transcriptional repressor of miR-34a that negatively controls the expression of miR-34a via a conserved STAT3-binding site in the first intron of the *MIR34A* gene (27), we speculated that KRAS might regulate miR-34a expression through PI3K-STAT3 signaling. To prove this hypothesis, we first measured STAT3 phosphorylation levels in the MEF cells; the p-STAT3 levels were higher in MEF^{G12C} and MEF^{G12D} cells than in the MEF^{WT} cells (Figure 6B and Supplementary Figure 11B, C). Moreover, overexpression of $KRAS^{G12C}$ or $KRAS^{G12D}$ but not $KRAS^{WT}$ increased the p-STAT3 levels in H358 and SK-LU-1 cells (Figure 6C, D and Supplementary Figure 11D-I). In contrast, KRAS knockdown decreased p-STAT3 in both cell lines (Figure 6E, F and Supplementary Figure 11J-O). We then determined the impact of MEK and PI3K inhibitors on STAT3 phosphorylation. Similar to the effect on miR-34a, the PI3K inhibitor but not the MEK inhibitor suppressed KRAS-driven STAT3

phosphorylation in both MEFs and H358 cells (Figure 6A and Supplementary Figure 11P, Q). Likewise, treatment with a STAT3 inhibitor (stattic) also caused sustained inhibition of STAT3 activation (Tyr705 phosphorylation) and CD47 expression as well as elevation of miR-34a in H358 cells (Supplementary Figure 12). Taken together, these data suggested that KRAS signaling could suppress miR-34a expression via the PI3K-STAT3 axis, which in turn relieves miR-34a-dependent repression of CD47, leading to escape from innate immune surveillance and tumor progression (Figure 6G).

KRAS mutation status is positively correlated with CD47 expression in several lung adenocarcinoma cohorts

To further explore the clinical relevance of our findings, we assessed the correlation of *KRAS* mutation status with CD47 expression in three independent lung adenocarcinoma cohorts. The first cohort was a commercial tissue microarray containing 157 pairs of lung adenocarcinoma and normal adjacent tissue samples, which lacked *KRAS* mutation information. We performed IHC analysis of CD47, p-STAT3 and p-AKT and found that CD47 levels were consistently higher in tumor tissues than in normal controls (Supplementary Figure 13A). High CD47 expression was also positively correlated with advanced tumor grade and poor survival (Supplementary Figure 13B, C). To evaluate the correlation of CD47 expression with KRAS signaling, we used the p-AKT level (downstream effector of PI3K) as a readout for KRAS activity and segregated all patient samples into high and low p-AKT groups. As expected, both CD47 and p-STAT3 levels were higher in the high p-AKT group than in the low p-AKT group (Figure 7A). Moreover, while high p-AKT expression was positively correlated with poor overall survival in lung adenocarcinoma patients, coordinated activation of KRAS (p-AKT^{high}) and

CD47 further increased the probability of a poor prognosis (Supplementary Figure 13D, E; hazard ratio 1.81 *vs.* 1.46).

In the second cohort, we performed IHC analysis of CD47 and p-STAT3 in a homemade tissue microarray containing paired tumor samples and adjacent normal tissue samples from 12 $KRAS^{MUT}$ lung adenocarcinoma patients and 28 $KRAS^{WT}$ lung adenocarcinoma patients. *KRAS* mutation status was determined by deep sequencing. In both $KRAS^{MUT}$ and $KRAS^{WT}$ patients, CD47 was highly expressed in the tumor samples compared with their normal counterparts (Supplementary Figure 13F). Compared with the $KRAS^{WT}$ tumors, the tumor samples with *KRAS* mutations displayed higher expression of CD47 and p-STAT3 (Figure 7B).

In the third cohort, we determined the *KRAS* mutation status and the expression levels of CD47, p-STAT3, and miR-34a in 100 pairs of lung adenocarcinoma and normal tissue samples. Thirty lung adenocarcinoma samples were confirmed to be *KRAS*-mutant and seventy were wild-type. The CD47 and p-STAT3 protein levels were consistently upregulated, and miR-34a downregulated in the lung adenocarcinoma samples compared with the paired normal controls, regardless of *KRAS* mutation status (Supplementary Figure 13G-I). In the tumor samples, the CD47 and p-STAT3 expression levels were much higher in the $KRAS^{MUT}$ patients than in the $KRAS^{WT}$ patients (Figure 7C, D). The opposite trend was observed for miR-34a (Figure 7E). The tight correlation between *KRAS* mutation status and CD47, p-STAT3, and miR-34a expression was further demonstrated by Pearson's correlation coefficient analysis, in which a reciprocal expression pattern between p-STAT3 and miR-34a and between CD47 and miR-34a, as well as a coincident pattern between p-STAT3 and CD47, were observed in the $KRAS^{MUT}$ patients but not

in the *KRAS*^{WT} patients (Figure 7F, G). In summary, these results from three independent lung adenocarcinoma cohorts were consistent with each other and confirmed that *KRAS* mutation status is positively correlated with CD47 expression in lung adenocarcinoma patients.

Targeted therapy against KRAS^{G12C} inhibits CD47 signaling and restores innate immune surveillance in animal models of lung cancer

From a translational perspective, the link between *KRAS* mutations and innate immune evasion suggests that targeting the KRAS-CD47 axis might compromise the ability of cancer cells to evade innate immune surveillance and increase their susceptibility to macrophage phagocytosis. In consistent with our hypothesis, treatment of the H358 human lung cancer cell line or the Lewis Lung Carcinoma (LLC, heterozygous for *Kras*^{G12C}) mouse lung cancer cell line with the FDA-approved KRAS^{G12C} inhibitor AMG 510 (28) attenuated KRAS activity, p-STAT3 and CD47 expression, enhanced miR-34a expression and stimulated macrophage-mediated phagocytosis in both H358 and LLC cells (Figure 8A-F and Supplementary Figure 14A-C). In addition, the PI3K agonist 740 Y-P but not the MAPK agonist PAF C-16 partially reversed the inhibitory effect of AMG 510 on p-STAT3 and CD47, further confirming the involvement of PI3K in KRAS regulation of STAT3 and CD47 (Supplementary Figure 15). Moreover, similar to the pharmacological inhibitors, when we used CRISPR/Cas9 to convert the genotype of the LLC mouse lung cancer cell line from *Kras*^{G12C} to *Kras*^{WT} and compared the phenotype between the isogenic cell pair LLC-Kras^{G12C} and LLC-Kras^{WT}, the later exhibited much lower levels of KRAS activity and CD47 expression, but much higher miR-34a and macrophage-mediated phagocytosis (Figure 8G-I and Supplementary Figure 14D, E).

Lastly, we tested the effect of AMG 510 on the tumor immune microenvironment in vivo. The LLC mouse lung cancer cells were injected via tail vein into immunocompetent C57BL/6 mice to establish a lung colonization model. AMG 510 treatment for 8 days significantly suppressed tumor growth, inhibited KRAS activity, STAT3 phosphorylation and CD47 expression, and stimulated miR-34a expression in tumor tissues (Figure 9A-E and Supplementary Figure 16A-E). Most importantly, AMG 510 treatment significantly increased the infiltration of M1 macrophages in the tumor tissue as well as tumor phagocytosis by the M1 macrophages (Figure 9F and Supplementary Figure 16F). Taken together, these data proved that the in vivo antitumor effect of $KRAS^{G12C}$ inhibitors might, at least in part, be due to the reactivation of the innate immune response to cancer cells.

DISCUSSION

Oncogenic *KRAS* mutations induce activation of the RAF-MEK-ERK and PI3K-AKT signaling pathways in a cell-autonomous manner, leading to constitutive activation of cell proliferation and inhibition of cell death; however, the role of KRAS signaling in the tumor microenvironment and tumor immune response is poorly understood. Our findings provide the first evidence that *KRAS* mutations could suppress the innate antitumor immune response by regulating CD47 expression in lung cancer cells. Thus, mutant KRAS communicates with macrophages via the CD47-SIRPα axis and renders tumor cells insensitive to phagocytosis by macrophages. Interestingly, two recent findings by Coelho et al. (12) and Canon et al. (13) demonstrated that *KRAS* mutations could also restrict the adaptive immune response through upregulation of PD-L1 and induce monoresistance to T cells. These findings complement each other and together indicate that mutant *KRAS* lies at the heart of tumor immune evasion - oncogenic KRAS signaling functions as a two-pronged approach to restrict the antitumor potential of both innate and adaptive immune systems. Inhibition of KRAS signaling could therefore render cancer cells more susceptible to immune attack by both T cells and macrophages, which might contribute to the overall antitumor effect of KRAS inhibitors in vivo. It is also reasonable to speculate that the combination of KRAS inhibitors and immune checkpoint inhibitors, including inhibitors of PD1/PD-L1 or CD47/SIRPα, could provide synergistic benefits to patients with *KRAS*-driven cancers.

Disrupting the CD47-SIRPα axis using anti-CD47 monoclonal antibodies has demonstrated efficacy in various preclinical models and has already entered phase I/II clinical trials (29, 30). However, two major obstacles may delay the clinical translation of anti-CD47 antibodies in cancer immunotherapy. First, predictive biomarkers of therapeutic response are underdeveloped.

In this study, we established a positive correlation between *KRAS* mutation status and CD47 overexpression in lung adenocarcinoma patients. Thus, *KRAS*-mutant lung adenocarcinoma patients might be especially sensitive to anti-CD47 immunotherapy. Second, due to the ubiquitous expression of CD47 in normal tissues, anti-CD47 antibodies may elicit severe side effects such as anemia, thrombocytopenia, and leukopenia, as observed in animal models (31, 32). The combination with KRAS inhibitors might help reduce the effective dose of anti-CD47 antibodies, thereby limiting the side effects and toxicities associated with anti-CD47 therapy. Altogether, a better understanding of how the KRAS-CD47 axis evades innate immune surveillance may provide a framework for patient selection and combination therapies to enhance the effectiveness of anti-CD47 immunotherapy.

Taken together, this study demonstrates that active KRAS can promote innate immune evasion of lung cancer through upregulation of CD47. These findings not only extend our understanding of the role of KRAS signaling in tumor immune surveillance but could also be exploited for the treatment of *KRAS*-driven cancers.

METHODS

Study design

For the *KRAS*-driven spontaneous lung cancer model, $Kras^{LSL\text{-}G12D/+}$ and $Kras^{LSL\text{-}G12D/+};p53^{flfl}$ transgenic mice were intratracheally administered Adeno-Cre to induce pulmonary adenocarcinoma formation. Tumor growth, CD47 expression, and macrophage infiltration were assessed at different time points or were evaluated when disrupting the KRAS-CD47 signaling axis. For the animal models of lung cancer, C57BL/6 mice were injected via tail vein with LLC cells ($Kras^{G12C}$) and administered the $KRAS^{G12C}$ inhibitor AMG 510 via oral gavage after tumor formation; then, tumor regression, CD47 expression and macrophage infiltration were assessed. For determination of the molecular mechanism underlying KRAS-mediated CD47 activation, a *Ras*-less MEF model stably overexpressing $KRAS^{G12C}$, $KRAS^{G12D}$ or $KRAS^{WT}$ and human lung cancer cell lines H358 ($KRAS^{G12C}$) and SK-LU-1 ($KRAS^{G12D}$) were cultured and assessed. For the in vitro phagocytosis assay, FACS and fluorescence microscopy were performed to analyze the phagocytosis of primary lung tumor cells or lung cancer cell lines by human peripheral blood monocyte-derived macrophages. For analysis of lung adenocarcinoma patient samples, the correlation of *KRAS* mutation status with CD47 expression was assessed in three independent lung adenocarcinoma cohorts.

Reagents

AMG 510, MEK inhibitor GSK1120212 (trametinib), PI3K inhibitor GDC-0941 (pictilisib) and PI3K agonist 740 Y-P (HY-P0175) were purchased from MedChemExpress (Shanghai, China); the STAT3 inhibitor stattic was purchased from Selleck (Houston, TX); the MAPK agonist PAF

C-16 (sc-201009) was purchased from Santa Cruz Biotechnology (Santa Cruz, CA). Unless noted, all chemicals were purchased from Sigma (St. Louis, MO).

Cell culture

The human lung cancer cell lines H358 and SK-LU-1 were obtained from the ATCC. The human embryonic kidney cell line HEK293T and mouse lung cancer cell line LLC were obtained from the Shanghai Institute of Cell Biology, Chinese Academy of Sciences (Shanghai, China). Cells were certified by STR analysis and regularly checked for mycoplasma contamination. *Ras*-less MEF cell lines overexpressing different KRAS mutations were obtained from the NIH RAS Initiative and cultured as indicated in https://www.cancer.gov/research/key-initiatives/ras/ras-central/blog/2017/rasless-mefs-drug-screens. H358 cells were maintained in RPMI 1640 medium (C11875500BT, Gibco, California, USA) supplemented with 10% FBS (10099-141, Gibco, Australia); SK-LU-1, LLC, and HEK293T cells were maintained in high-glucose (4.5 g/L) DMEM (C11995500BT, Gibco) supplemented with 10% FBS (Gibco). All cells were incubated in 5% CO_2 at 37°C in a humidified atmosphere.

Construction of an LLC-Kras^{WT} cell line using CRISPR/Cas9

A *Kras* gene-modified LLC cell line (LLC-Kras^{WT}) was developed using the GenCRISPR gene editing kit from Genscript (Nanjing, China). Briefly, based on the genomic sequences of the parental LLC cell line harboring a heterozygous *Kras^{G12C}* mutation (LLC-Kras^{G12C}), several gRNA sequences (best one: GACTGAGTATAAACTTGTGG) were designed targeting the area near the *Kras^{G12C}* site, and a donor template was designed containing the designated mutation.

By transient co-transfection of plasmids carrying the gRNA-Cas9 plasmid and donor plasmid, the *Kras* gene was targeted and mutated from G12C to WT. Single clones with successful gene conversion were selected by limiting dilution and expansion in 96-well plates and verified by Sanger sequencing.

Patient tissue samples

A total of four separate patient cohorts were used in this study. For the assessment of macrophage phagocytosis and CD47 expression in fresh human lung adenocarcinoma tissues, 18 pairs of tumor and normal adjacent tissue samples were collected from lung adenocarcinoma patients receiving surgery at the Jiangsu Cancer Hospital, China. Briefly, tissues were placed in 1.0 mL RPMI 1640 with Liberase TL (0.2 mg/ml; Roche) and DNase I (20 μg/ml; Ambion), and minced with scissors to sub-millimeter pieces. Tissues were then dissociated into single cells using the gentleMACS program at 37℃ for 40 min, according to the manufacturer's instructions. Cells were then passed through a 70 mm mesh and centrifuged at 350 g for 5 min. Cell pellets were re-suspended and one aliquot of the cells (1×10^6) were incubated with 1 mg of fluorescently conjugated mAbs against human CD47 (BD Biosciences) or the isotype control. Another aliquot of the cells was subjected to the in vitro phagocytosis assay. Samples were fixed in 4% paraformaldehyde, washed, re-suspended in FACS buffer, and analyzed by flow cytometry (FACScalibur, BD Biosciences).

Three patient cohorts were used for the correlation analysis of *KRAS* mutation and CD47 levels. The first cohort was a commercial tissue microarray containing 157 pairs of lung

adenocarcinoma and normal adjacent tissue samples purchased from Shanghai Outdo Biotech (Shanghai, China). The second cohort was a homemade tissue microarray containing 12 pairs of $KRAS^{MUT}$ lung adenocarcinoma and adjacent normal tissue samples and 28 pairs of $KRAS^{WT}$ lung adenocarcinoma and adjacent normal tissue samples; these samples were obtained from Jiangsu Biobank of Clinical Resources (located at Jiangsu Cancer Hospital, Nanjing, China). The third cohort containing 100 pairs of lung adenocarcinoma and normal adjacent tissue samples were obtained from the Jiangsu Biobank of Clinical Resources (located at Jiangsu Cancer Hospital, Nanjing, China. These cases were selected based on a clear pathological diagnosis. Approximately 5 g segments of lung adenocarcinoma and normal tissues were promptly transferred to containers with liquid nitrogen and frozen at -80°C. The *KRAS* mutation status in these samples was determined by TA cloning and sequencing of RT-PCR products. Patient information is shown in Supplementary Table 2.

Genetic models of lung cancer

The $Kras^{LSL\text{-}G12D/+}$ and $Kras^{LSL\text{-}G12D/+};p53^{flfl}$ transgenic mice were originally generously provided by Professor Hongbin Ji (Shanghai Institutes for Biological Sciences). The mice were maintained on a 12 h light/dark cycle (lights on at 7 am) with free access to food and water. All animal care and handling procedures were performed in accordance with the National Institutes of Health's Guide for the Care and Use of Laboratory Animals and were approved by the Ethical Committee of Nanjing University (Nanjing, China). For $KRAS^{G12D}$ activation in mouse lungs, six-week-old $Kras^{LSL\text{-}G12D/+}$ and $Kras^{LSL\text{-}G12D/+};p53^{flfl}$ mice were first anaesthetized with sodium pentobarbital, then 5×10^6 plaque-forming units of Adeno-Cre were diluted with PBS to obtain a final volume of 50 μL and given through intratracheal administration (21, 22). At different time points after

Adeno-Cre administration (0 and 5 months for *Kras*$^{LSL\text{-}G12D/+}$ mice and 0, 1 and 3 months for *Kras*$^{LSL\text{-}G12D/+}$;*p53*^{flfl} mice), the mice were anaesthetized to evaluate tumor growth by microcomputed tomography (micro-CT) scanning or euthanized to confirm lung adenocarcinoma formation by histological analysis. Histological analysis was performed by hematoxylin and eosin (H&E) staining. Excised lung adenocarcinomas were also processed to determine CD47 expression, macrophage infiltration by western blotting, immunofluorescence staining or IHC analyses.

For AAV-mediated silencing of *Cd47*, a short hairpin RNA of *Cd47* was cloned into the AAV vector AAV9-CAG-EGFP (Sunbio, Shanghai, China) (AAV-*Cd47* shRNA). An AAV encoding scrambled shRNA (AAV-control shRNA) served as the negative control. *Kras*$^{LSL\text{-}G12D/+}$;*p53*^{flfl} mice were intratracheally co-administered with Adeno-Cre along with the AAV-control shRNA or AAV-*Cd47* shRNA. Then, the mice were divided into 2 groups and monitored to determine either survival time or tumor regression. For survival analysis, the mice were monitored for 150 days without any further treatment. For tumor size, the mice were anaesthetized to evaluate tumor growth by micro-CT scanning or euthanized to confirm lung adenocarcinoma formation by histological analysis at 90 days. Excised lung adenocarcinomas were also processed to determine CD47 expression and macrophage infiltration by western blotting, immunofluorescence staining or IHC analysis.

For the overexpression of miR-34a in mice, an AAV9-CAG-EGFP (Sunbio) encoding miR-34a (AAV-miR-34a) was used, with or without simultaneous administration of an AAV9-CAG-EGFP (Sunbio) expressing the CD47 open reading frame (AAV-CD47). An AAV encoding

scrambled RNA (AAV-scrRNA) served as the negative control of AAV-miR-34a, and an AAV that does not express a transgene (AAV-control) served as the negative control of AAV-CD47. The *Kras*$^{LSL\text{-}G12D/+}$*;p53*^{flfl} mice were intratracheally co-administered Adeno-Cre along with the combination of AAV-scrRNA plus AAV-control, AAV-miR-34a plus AAV-control or AAV-miR-34a plus AAV-CD47. The mice were assessed as described above.

Animal models of lung cancer

To generate a lung colonization model of human lung cancer, 5×10^6 H358 cells stably transfected with eGFP were intravenously injected into BALB/c nude mice via the tail vein. After 3 weeks, one mouse was euthanatized every week to ensure successful lung tumor formation by immunofluorescence. Then, the tumor-bearing mice were divided into three groups and monitored to determine macrophage infiltration by immunofluorescence at different times.

To generate a lung colonization model of lung cancer in immune competent mice, 5×10^6 LLC cells were intravenously injected into C57BL/6 mice via the tail vein. After 15 days, the mice were monitored using non-invasive micro-CT scanning to ensure successful tumor formation in the lungs. Then, the tumor-bearing mice were randomly divided into two groups and were orally administered with 100 mg/kg AMG 510 or vehicle control. After 8 days, the mice were euthanized to evaluate lung tumor burden by histopathological staining. Excised lung tumors were also processed to determine CD47 expression and macrophage infiltration by western blotting, immunofluorescence staining or IHC analyses. Moreover, single cell suspensions of tumors were prepared for flow cytometry as described previously. Briefly, tumors were placed in

1.0 mL RPMI 1640 with Liberase TL (0.2 mg/ml; Roche) and DNase I (20 μg/ml; Ambion), and minced with scissors to sub-millimeter pieces. Tissues were homogenized in the MACS tissue homogenizer using the gentleMACS program according to the manufacturer's instructions and then incubated at 37℃ for 40 min. Specimens were passed through a 70 mm mesh and centrifuged at 350 g for 5 min. Cell pellets were resuspended and cell labelling was performed by incubating 1×10^6 cells with 0.5 μg of fluorescently conjugated antibodies directed against mouse F4/80 (BD Biosciences). Intracellular iNOS antibody (BD Biosciences) staining was performed following the intracellular staining protocol. Samples were fixed in 4% paraformaldehyde, washed, resuspended in FACS buffer, and analyzed by flow cytometry (FACScalibur, BD Biosciences).

Micro-CT scanning

Micro-CT analysis was performed to assess lung tumor growth because the micro-CT images clearly distinguished the lung tumors from the surrounding tissue even without any contrast agent, and the reconstructed 3-D pulmonary images can easily differentiate the tumors from the blood vessels (33). Briefly, micro-CT scans were performed using a SkyScan 1176 micro-CT analyzer, which scanned a 360° area at a resolution of 50 μm with a rotation step of 0.5. The system comprised two metallochromic tubes equipped with a fixed 0.5 mm Al filter and two 1280 × 1024 pixel digital X-ray cameras. Images were acquired at 60 kV and 134 μA. The mice were scanned while in a supine position. The micro-CT data were batch-sorted, processed, and reconstructed as 3-D pulmonary images using the N-Recon program according to the manufacturer's instructions (SkyScan). The reconstructed data were subsequently imaged using

DataViewer, and the tumor numbers and volumes were calculated using the CTAn program according to the manufacturer's instructions (SkyScan, Nanjing, China).

Histopathology

For histopathological examination of the *Kras*$^{LSL\text{-}G12D/+}$ and *Kras*$^{LSL\text{-}G12D/+}$;*p53*$^{fl/fl}$ mice, whole lung lobes were fixed in 4% paraformaldehyde overnight and embedded in paraffin. H&E staining was performed with a standard method. Digitally scanned images of H&E slides were created with the Aperio ScanScope AT2 at 20 × magnification and analyzed with Aperio's WebScope software. For quantification of the tumor burden, tumor regions were outlined, and the percentage of the tumor area relative to the total lung area was calculated for each mouse. All tumor burdens were assessed in a blinded fashion, and at least five mice per group were included in the analyses.

Immunofluorescence staining

Excised lung adenocarcinomas were postfixed for 4 h in 4% PFA and cryoprotected in 20% and 30% sucrose in 1 × PBS at 4°C. For immunofluorescence analysis, the sections were postfixed for 10 min in 4% PFA and then washed with 1 × PBS prior to blocking with 5% normal horse serum/0.25% Triton X-100 in PBS (1 h). The sections were then incubated with CD11b, iNOS, TNF-α or KRAS^{G12D} primary antibodies diluted 1:100 in blocking solution overnight. Detailed information on the primary antibodies used can be found in Supplementary Table 3. The following day, the sections were washed with 1 × PBS and subsequently incubated in blocking solution containing secondary antibody for 1 h. Then, the sections were washed with 1 × PBS

and placed in DAPI staining solution for 10 min. After the sections were washed with 1 × PBS, they were examined with a TCS SP8 inverted laser scanning confocal microscope (Leica). Digital images from the microscope were recorded with LAS X Viewer Software (Leica). Cell counts were performed using Image-Pro Plus 6.0 software (Media Cybernetics, Inc., Rockville, MD) in combination with manual scoring to ensure accuracy.

Immunohistochemistry

IHC was performed according to standard protocols. Prior to staining, sections from the lung tumors of the $Kras^{LSL\text{-}G12D/+}$ and $Kras^{LSL\text{-}G12D/+};p53^{fl/fl}$ mice were baked at 60°C for 1 h, deparaffinized in xylene and rehydrated through graded ethanol. Antigen retrieval was performed by heating the sections under high pressure in citrate antigen retrieval solution for approximately 5 min. The sections were incubated with monoclonal antibodies against CD47, iNOS, TNF-α, p-AKT or p-STAT3 for 60 min at room temperature. Detailed information on the primary antibodies used can be found in Supplementary Table 3. The immunoreaction was detected by treatment with diaminobenzidine chromogen for 3 min. The immunoreaction images were viewed and captured using the NDP.view.2 software program. Protein expression was assessed by two experienced pathologists blinded to the clinical data who performed the first reading independently and then debated any discrepancies until reaching a consensus.

Small RNA sequencing

Small RNA deep sequencing was performed to examine the miRNA profiles in the lung tumors of the $Kras^{LSL\text{-}G12D/+}$ mice. All sRNA library construction and deep sequencing were performed

by Novogene (Beijing, China). Briefly, sRNA libraries were constructed using the NEBNext Multiplex Small RNA Library Prep Set for Illumina (NEB, USA). After library quality validation, raw data for each sRNA library were generated on the Illumina HiSeq 2500 platform. The clean reads were obtained after data filtration. Precursor and mature miRNA sequences were obtained from miRBase v21. To annotate miRNA, clean reads were mapped to known mouse miRNA precursor sequences by using bowtie and only candidates with no more than 1 mismatch and 2 shifts were counted as miRNA matches. Differential analysis was performed using DESeq2. Significance was set at uncorrected $p < 0.05$ for broad pattern identification. A fold-change threshold was set at > 2. Volcano plot was generated using the ggplot2 R package and heatmap were generated using the pheatmap R package. The raw sequence data reported in this paper have been deposited in the Genome Sequence Archive in National Genomics Data Center, China National Center for Bioinformation/Beijing Institute of Genomics, Chinese Academy of Sciences (GSA: CRA008806) that are publicly accessible at https://ngdc.cncb.ac.cn/gsa.

Cell transfection

Sequences of the open reading frames of wild-type *KRAS* (*KRAS*^{WT}) or mutant *KRAS*^{G12C} or mutant *KRAS*^{G12D} were synthetized by GenScript (Nanjing, China) and inserted into a CMV-EGFP plasmid. A plasmid that does not express a transgene served as the negative control. *KRAS* siRNAs were purchased from GenePharma (Shanghai, China). A siRNA with a scrambled sequence served as the negative control. MiR-34a mimic and antisense were purchased from GenePharma. Control mimic and antisense designed to express double-stranded or single-stranded scrambled RNAs served as negative controls. H358 and SK-LU-1 cells were seeded in 12-well plates, and each well was transfected with 5 μg of the *KRAS*^{WT}, *KRAS*^{G12C} or *KRAS*^{G12D}

plasmids or 50 pmol of miR-34a mimic, miR-34a antisense or the corresponding negative controls by Lipofectamine 3000 (Invitrogen) according to the manufacturer's instructions. Total RNA and protein were isolated 24 or 48 h after transfection. Sequences of synthetic siRNAs, miRNA mimics and antisense strands are listed in Supplementary Table 4.

RNA isolation and quantitative RT-PCR assay

Total RNA extraction, reverse transcription and TaqMan-based real-time PCR were performed as described previously. Briefly, total RNA was extracted from cultured cells and mouse tumors with TRIzol Reagent (Invitrogen, Carlsbad, CA) according to the manufacturer's instructions.

For quantitative RT-PCR analysis of miRNAs, 100 ng of total RNA was reverse transcribed to cDNA using AMV reverse transcriptase (TaKaRa, Dalian, China) and stem-loop RT primers (Applied Biosystems, Foster City, CA). The following reaction conditions were used: 16°C for 30 min, 42°C for 30 min, and 85°C for 5 min. Real-time RT-PCR was performed using TaqMan miRNA probes (Applied Biosystems) on an Applied Biosystems 7300 Sequence Detection System (Applied Biosystems). The reactions were incubated in a 96-well optical plate at 95°C for 10 min followed by 40 cycles at 95°C for 15 s and 60°C for 1 min. All reactions were run in triplicate. After the reactions were complete, the cycle threshold (C_T) values were determined using fixed threshold settings, and the mean C_T was determined from triplicate PCRs. The relative expression of miRNAs was determined using the $2^{-\triangle\triangle CT}$ method, and U6 snRNA served as the internal control.

For mRNA analysis, 1 μg of total RNA was reverse transcribed to cDNA using AMV reverse transcriptase (TaKaRa) and oligo dT primer (TaKaRa). The following reaction conditions were used: 16°C for 30 min, 42°C for 30 min, and 85°C for 5 min. Real-time RT-PCR was performed using SYBR™ Green PCR Master Mix (Invitrogen, Carlsbad, CA, USA) on an Applied Biosystems 7300 Sequence Detection System. The reactions were incubated in a 96-well optical plate at 95°C for 10 min followed by 40 cycles at 95°C for 15 s and 60°C for 1 min. All reactions were run in triplicate. After the reactions were complete, the C_T values were determined using fixed threshold settings, and the mean C_T was determined from the triplicate PCRs. The relative expression of mRNAs was determined using the $2^{-\triangle\triangle CT}$ method, and β-actin mRNA served as the internal control. The primer sequences are listed in Supplementary Table 5.

Protein extraction and western blotting

Cells were rinsed with cold PBS (pH 7.4) and then lysed in RIPA buffer (0.5% NP-40, 0.1% sodium deoxycholate, 150 mM NaCl and 50 mM Tris-HCl, pH 7.5) supplemented with a protease and phosphatase inhibitor cocktail (Thermo Scientific, Rockford, IL) on ice for 30 min. The tissue samples were flash frozen in liquid nitrogen, ground into powder and then lysed in RIPA buffer. The cell lysates and tissue homogenates were centrifuged for 10 min (12,000 × g at 4°C), the supernatant was collected, and the protein concentration was determined using a Pierce BCA Protein Assay Kit (Thermo Scientific). Equal amounts of protein (30-60 μg) were resolved via 10%–12.5% SDS-PAGE and then transferred to a PVDF membrane (Millipore, Bedford, MA). The membrane was blocked in Tris-buffered saline Tween-20 (TBST) containing 5% bovine serum albumin and then incubated with the corresponding primary antibodies overnight at 4°C. After a 1 h incubation with HRP-conjugated secondary antibody, the protein level was

detected using a luminal reagent. The data were quantified using ImageJ software (NIH, Bethesda, MD), and relative protein expression was normalized to the value of GAPDH. Information on primary antibodies is listed in Supplementary Table 3.

For analyses of 3 different proteins (CD47, p-STAT3 and STAT3) and 1 internal control (GAPDH) in the same samples, sliced bands from the same blot were used. Based on the apparent molecular weights of CD47, p-STAT3, STAT3 and GAPDH (40~70, ~88, ~88 and 37 kD), the PVDF membrane was cut at 40 kD and 70 kD into three parts (< 40 kD, 40~70 kD and > 70 kD). The three parts were then first blotted with CD47 (40~70 kD), p-STAT3 (~88 kD) and GAPDH (37 kD) primary antibodies and detected with a secondary antibody. The upper PVDF membrane (> 70 kD) were then treated with antibody removal solution (Beyotime Biotechnology) to remove both primary and secondary antibodies and blotted with a STAT3 (~88 kD) antibody. For analysis of KRAS (21 kD), p-STAT3 and STAT3 in the same samples, the PVDF membrane was cut at 35 kD and 70 kD into three parts (< 35 kD, 35~70 kD and > 70 kD). The three parts were then first blotted with KRAS (21 kD), p-STAT3 (~88 kD) and GAPDH (37 kD); the upper PVDF membrane (> 70 kD) were then stripped and blotted with STAT3 (~88 kD) antibody. The same experiment was repeated three times, and in each biological replicate, the sliced membranes were stripped only once (blotted twice).

Luciferase reporter assay

For analysis of the direct binding of miR-34a to CD47, the 3'-UTR of CD47 was inserted into a firefly luciferase reporter plasmid (GenScript, Nanjing, China). For determination of the binding

specificity, sequences that interacted with the miR-34a seed sequence were mutated from ACTGCC, CACTGCC and ACTGCC to TGACGG, GTGACGG and TGACGG, respectively, and the mutant CD47 3'-UTR fragment was inserted into the same reporter plasmid. The β-galactosidase (β-gal) plasmid was included as a transfection control. In the luciferase assay, HEK293T cells were cultured in DMEM containing 10% FBS and seeded in 24-well plates. At 24 h after plating, 0.2 μg of wild-type or mutant luciferase reporter plasmid, 0.1 μg of β-gal plasmid and equal amounts (20 pmol) of miR-34a mimic or control mimic (GenePharma) were co-transfected into cells with Lipofectamine 2000 (Invitrogen) according to the manufacturer's instructions. At 24 h post-transfection, the cells were analyzed using a luciferase assay kit (Cat# E4550, Promega, Madison, WI) to determine the fluorescence intensity. All experiments were performed in triplicate wells for each condition and repeated three times independently.

In vitro phagocytosis assay

Peripheral blood mononuclear cells (PBMCs) were isolated via density gradient centrifugation using Ficoll-Hypaque (GE Healthcare) from healthy donors. $CD14^+$ monocytes were isolated by magnetic column purification based on positive selection with anti-CD14 microbeads (Miltenyi Biotec) with a purity of 96%. Then, 1×10^6 $CD14^+$ cells were cultured in RPMI 1640 medium supplemented with 2 mmol/mL glutamine, 100 μg/mL ticarpen and 10% FBS (complete RPMI) and stimulated with granulocyte-macrophage colony stimulating factor (GM-CSF) at 25 ng/mL for 7 days to generate macrophages.

The phagocytosis assay was conducted as previously described (19, 34). Briefly, macrophages were plated at a density of 5×10^4 cells per well in a 24-well tissue-culture plate in complete DMEM supplemented with GM-CSF overnight before the experiment. H358 cells were pre-transfected with *KRAS*^{G12C} plasmid, miR-34a mimic or *CD47* plasmid and their corresponding negative controls for 48 h and then stained with 2.5 μM carboxyfluorescein succinimidyl ester (CFSE) at 37°C for 10 min. Macrophages were incubated in serum-free medium for 2 h before addition of 2×10^5 CFSE-labeled H358 cells. After coculture for 2 h at 37°C, the cells were harvested, the macrophages were stained with APC-labeled anti-F4/80 antibody (BD Biosciences), and flow cytometry (FACScalibur, BD Biosciences) was performed to detect $CFSE^+F4/80^+$ cells. A total of 10,000 cells in each sample were analyzed. Phagocytosis was calculated as the percentage of $CFSE^+F4/80^+$ cells (Q2) among $CFSE^+$ cells (Q1+Q2): phagocytosis (%) = [Q2/(Q1+Q2)] ×100%.

For direct visualization of the phagocytosed H358 cells by macrophages, a phagocytosis assay was performed by fluorescence microscopy (35). Briefly, a GFP-encoding lentivirus was prepared from the pCDH-CMV construct using standard techniques and transfected into H358 cells to generate GFP^+ cells. Macrophages were plated at a density of 5×10^4 cells per well in a 24-well tissue culture plate. GFP^+ H358 cells were pre-transfected with *KRAS*^{G12C} plasmid, miR-34a mimic or *CD47* plasmid and their corresponding negative controls for 48 h. Macrophages were incubated in serum-free medium for 2 h. Then, 2×10^4 GFP^+ H358 cells were added to the macrophage-containing wells and incubated for 2 h at 37°C. Macrophages were repeatedly washed and subsequently examined by fluorescence microscopy (Leica DMI6000B). Macrophages that were GFP^+ represent macrophages containing phagocytosed

H358 cells. The phagocytic index was calculated as the number of phagocytosed GFP^+ cells per 100 macrophages.

IHC analysis in tissue microarray

Commercial tissue microarray chips containing 157 pairs of lung adenocarcinoma samples and normal adjacent tissue (NAT) samples were purchased from Shanghai Outdo Biotech (Shanghai, China). Each sample dot with a diameter of 1.5 mm and a thickness of 4 μm was prepared according to a standard method. All patients had been pathologically diagnosed with adenocarcinoma after operation, and follow-up data (range 0–120 months) were available. Informed consent was obtained for all patients. The IHC analysis was performed as described previously (36). Briefly, the tissue sections were blocked with goat serum and then incubated with anti-CD47 (1:100, Abcam, ab175388), anti-p-STAT3 (1:100, 9145S, Cell Signaling Technology, MA, USA) or anti-p-AKT (1:100, 4066S, Cell Signaling Technology) antibodies overnight at 4°C. The sections were stained with 3,3-diaminobenzidine and counterstained with hematoxylin after being incubated with secondary antibody. All IHC sample dots were assessed by two independent pathologists blinded to both the sample origins and the subject outcomes. Both staining intensity and positive percentage were used to examine the expression of CD47, p-STAT3 and p-AKT in the lung cancer tissues: the IHC staining score was scored according to the extent of cell staining (≤ 10% positive cells for 0; 11%–50% positive cells for 2; 51%–80% positive cells for 3; > 80% positive cells for 4) and the staining intensity (no staining for 0; slight staining for 1; moderate staining for 2; strong staining for 3). Scores for the percentage of positive cells and the staining intensity were added. The CD47, p-STAT3 and p-AKT expression levels in the lung adenocarcinoma tissues were considered medium expression when the score of

each protein was in the range of average score ± 20% in all samples; high expression was considered higher than medium expression; low expression was considered lower than medium expression. Patient information related to the tissue microarray is shown in Supplementary Table 2.

In addition, a tissue microarray containing 12 pairs of $KRAS^{MUT}$ lung adenocarcinoma and normal adjacent tissue samples and 28 pairs of $KRAS^{WT}$ lung adenocarcinoma and normal adjacent tissue samples was obtained from the Jiangsu Biobank of Clinical Resources. All patients had been pathologically diagnosed with adenocarcinoma after operation, and informed consent was obtained for all patients. IHC analysis in the tissue microarray was performed with anti-CD47 and anti-p-STAT3 antibodies as described above. Patient information related to the tissue microarray is shown in Supplementary Table 2.

Statistical analysis

All statistical tests were performed using the open-source statistics package R or using GraphPad Prism software 8 (San Diego, CA). Data are presented as the mean ± SEM. Differences were considered statistically significant at $p < 0.05$. Normality and equal variances between group samples were assessed using the Shapiro-Wilk test and Brown–Forsythe tests, respectively. When normality and equal variance were achieved between sample groups, one-way ANOVA (followed by Bonferroni's multiple comparisons test), two-way ANOVA (followed by Bonferroni's multiple comparisons test) or t-tests were used. Where normality or equal variance

of samples failed, Kruskal–Wallis one-way ANOVA (followed by Dunn's correction) or Mann–Whitney U tests were performed.

Study approval

All patient samples were obtained from Jiangsu Biobank of Clinical Resources (located at Jiangsu Cancer Hospital, Nanjing, China). These samples were collected from lung adenocarcinoma patients receiving surgery at the Jiangsu Cancer Hospital, China. Informed consent was obtained from each patient, and the collection of tissue specimens was approved by the Internal Review and Ethics Boards at Jiangsu Cancer Hospital. All animal care and handling procedures were performed in accordance with the National Institutes of Health's Guide for the Care and Use of Laboratory Animals and were approved by the Ethical Committee of Nanjing University (Nanjing, China).

ACKNOWLEDGEMENTS:

We thank Dr. Hongbin Ji (CAS Center for Excellence in Molecular Cell Science, Shanghai, China) for kindly providing the *Kas*$^{LSL\text{-}G12D/+}$ and *Kras*$^{LSL\text{-}G12D/+}$;*p53*$^{fl/fl}$ mice.

AUTHOR CONTRIBUTIONS:

Conceptualization: XC, CY, RY;

Methodology: HH, RC, YW, XW, JW, YK, SZ, ZZ, HZ, RY, GL, QW, XZ;

Investigation: HH, RC, YW, XW, JW, YK, SZ, ZZ, HZ, RY, GL, QW, XZ;

Visualization: HH, RC, YW;

Funding acquisition: XC, CY, RY;

Project administration: XC, CY, RY;

Supervision: XC, CY, RY;

Writing – original draft: HH, RC;

Writing – review & editing: XC, CY, CYZ.

The order of co-first authors was determined by the time they got involved in this project.

FUNDING:

National Natural Science Foundation of China grant 21877060 (CY)

National Natural Science Foundation of China grant 32022015 (XC)

National Natural Science Foundation of China grant 31871295 (XC)

Starry Night Science Fund of Zhejiang University Shanghai Institute for Advanced Study SN-ZJU-SIAS-008 (CY and XC)

Fundamental Research Funds for the Central Universities 020814380146 (XC)

Fundamental Research Funds for the Central Universities 020814380162 (XC)

Fundamental Research Funds for the Central Universities 020814380178 (CY)

REFERENCES

1. Moore AR, et al. RAS-targeted therapies: is the undruggable drugged? *Nat Rev Drug Discov.* 2020;19(8):533-52.
2. Simanshu DK, et al. RAS proteins and their regulators in human disease. *Cell.* 2017;170(1):17-33.
3. Pylayeva-Gupta Y, et al. RAS oncogenes: weaving a tumorigenic web. *Nature Reviews Cancer.* 2011;11(11):761-74.
4. Collisson EA, et al. Comprehensive molecular profiling of lung adenocarcinoma. *Nature.* 2014;511(7511):543-50.
5. Drosten M, Barbacid M. Targeting the MAPK pathway in KRAS-driven tumors. *Cancer Cell.* 2020;37(4):543-50.
6. Schwartz S, et al. Feedback suppression of PI3K alpha signaling in PTEN-mutated tumors is relieved by selective inhibition of PI3K beta. *Cancer Cell.* 2015;27(1):109-22.
7. Cox AD, et al. Drugging the undruggable RAS: Mission Possible? *Nat Rev Drug Discov.* 2014;13(11):828-51.
8. Papke B, Der CJ. Drugging RAS: Know the enemy. *Science.* 2017;355(6330):1158-63.
9. Brown EJ, Frazier WA. Integrin-associated protein (CD47) and its ligands. *Trends Cell Biol.* 2001;11(3):130-5.
10. Chao MP, et al. Programmed cell removal: a new obstacle in the road to developing cancer. *Nature Reviews Cancer.* 2012;12(1):58-67.
11. Gardai SJ, et al. Cell-surface calreticulin initiates clearance of viable or apoptotic cells through trans-activation of LRP on the phagocyte. *Cell.* 2005;123(2):321-34.

12. Coelho MA, et al. Oncogenic RAS signaling promotes tumor immunoresistance by stabilizing PD-L1 mRNA. *Immunity.* 2017;47(6):1083-99.e6.

13. Canon J, et al. The clinical KRAS(G12C) inhibitor AMG 510 drives anti-tumour immunity. *Nature.* 2019;575(7781):217-23.

14. Mantovani A, Sica A. Macrophages, innate immunity and cancer: balance, tolerance, and diversity. *Current Opinion in Immunology.* 2010;22(2):231-7.

15. Barclay AN, van den Berg TK. The interaction between signal regulatory protein alpha (SIRPα) and CD47: structure, function, and theraputic target. *Annual Review of Immunology*. 2014;32:25-50.

16. Chan KS, et al. Identification, molecular characterization, clinical prognosis, and therapeutic targeting of human bladder tumor-initiating cells. *Proceedings of the National Academy of Sciences of the United States of America.* 2009;106(33):14016-21.

17. Majeti R, et al. CD47 is an adverse prognostic factor and therapeutic antibody target on human acute myeloid leukemia stem cells. *Cell.* 2009;138(2):286-99.

18. Danielsen JMR, et al. Dysregulation of CD47 and the ligands thrombospondin 1 and 2 in multiple myeloma. *British Journal of Haematology.* 2007;138(6):756-60.

19. Willingham SB, et al. The CD47-signal regulatory protein alpha (SIRPa) interaction is a therapeutic target for human solid tumors. *Proceedings of the National Academy of Sciences of the United States of America.* 2012;109(17):6662-7.

20. Subbiah V, et al. A phase 2, multiarm study of anti-CD47 antibody, magrolimab, in combination with docetaxel in patients with locally advanced or metastatic solid tumors. *J Clin Oncol.* 2022;40(6).

21. DuPage M, et al. Conditional mouse lung cancer models using adenoviral or lentiviral delivery of Cre recombinase. *Nat Protoc.* 2009;4(7):1064-72.

22. Johnson L, et al. Somatic activation of the K-ras oncogene causes early onset lung cancer in mice. *Nature.* 2001;410(6832):1111-6.

23. Drosten M, et al. Genetic analysis of Ras signalling pathways in cell proliferation, migration and survival. *Embo J.* 2010;29(6):1091-104.

24. Anand S, et al. MicroRNA-132-mediated loss of p120RasGAP activates the endothelium to facilitate pathological angiogenesis. *Nat Med.* 2010;16(8):909-14.

25. Vogt PK, Hart JR. PI3K and STAT3: A new alliance. *Cancer Discov.* 2011;1(6):481-6.

26. Hart JR, et al. Essential role of Stat3 in PI3K-induced oncogenic transformation. *Proceedings of the National Academy of Sciences of the United States of America.* 2011;108(32):13247-52.

27. Rokavec M, et al. IL-6R/STAT3/miR-34a feedback loop promotes EMT-mediated colorectal cancer invasion and metastasis. *J Clin Invest.* 2014;124(4):1853-67.

28. Lanman BA, et al. Discovery of a covalent inhibitor of KRAS(G12C) (AMG 510) for the treatment of solid tumors. *J Med Chem.* 2020;63(1):52-65.

29. Fisher GA, et al. A phase Ib/II study of the anti-CD47 antibody magrolimab with cetuximab in solid tumor and colorectal cancer patients. *J Clin Oncol.* 2020;38(4).

30. Sikic BI, et al. First-in-human, First-in-class phase I trial of the anti-CD47 antibody hu5F9-G4 in patients with advanced cancers. *J Clin Oncol.* 2019;37(12):946-53.

31. Kuriyama T, et al. Engulfment of hematopoietic stem cells caused by down-regulation of CD47 is critical in the pathogenesis of hemophagocytic lymphohistiocytosis. *Blood.* 2012;120(19):4058-67.

32. Oldenborg PA, et al. Role of CD47 as a marker of self on red blood cells. *Science.* 2000;288(5473):2051-4.

33. Kumar MS, et al. The GATA2 transcriptional network is requisite for RAS oncogene-driven non-small cell lung cancer. *Cell.* 2012;149(3):642-55.

34. Zhang HM, et al. HIF-1 regulates CD47 expression in breast cancer cells to promote evasion of phagocytosis and maintenance of cancer stem cells. *Proceedings of the National Academy of Sciences of the United States of America.* 2015;112(45):E6215-E23.

35. Jaiswal S, et al. CD47 is upregulated on circulating hematopoietic stem cells and leukemia cells to avoid phagocytosis. *Cell.* 2009;138(2):271-85.

36. Huang JZ, et al. A peptide encoded by a putative lncRNA HOXB-AS3 suppresses colon cancer growth. *Mol Cell.* 2017;68(1):171-84.e6.

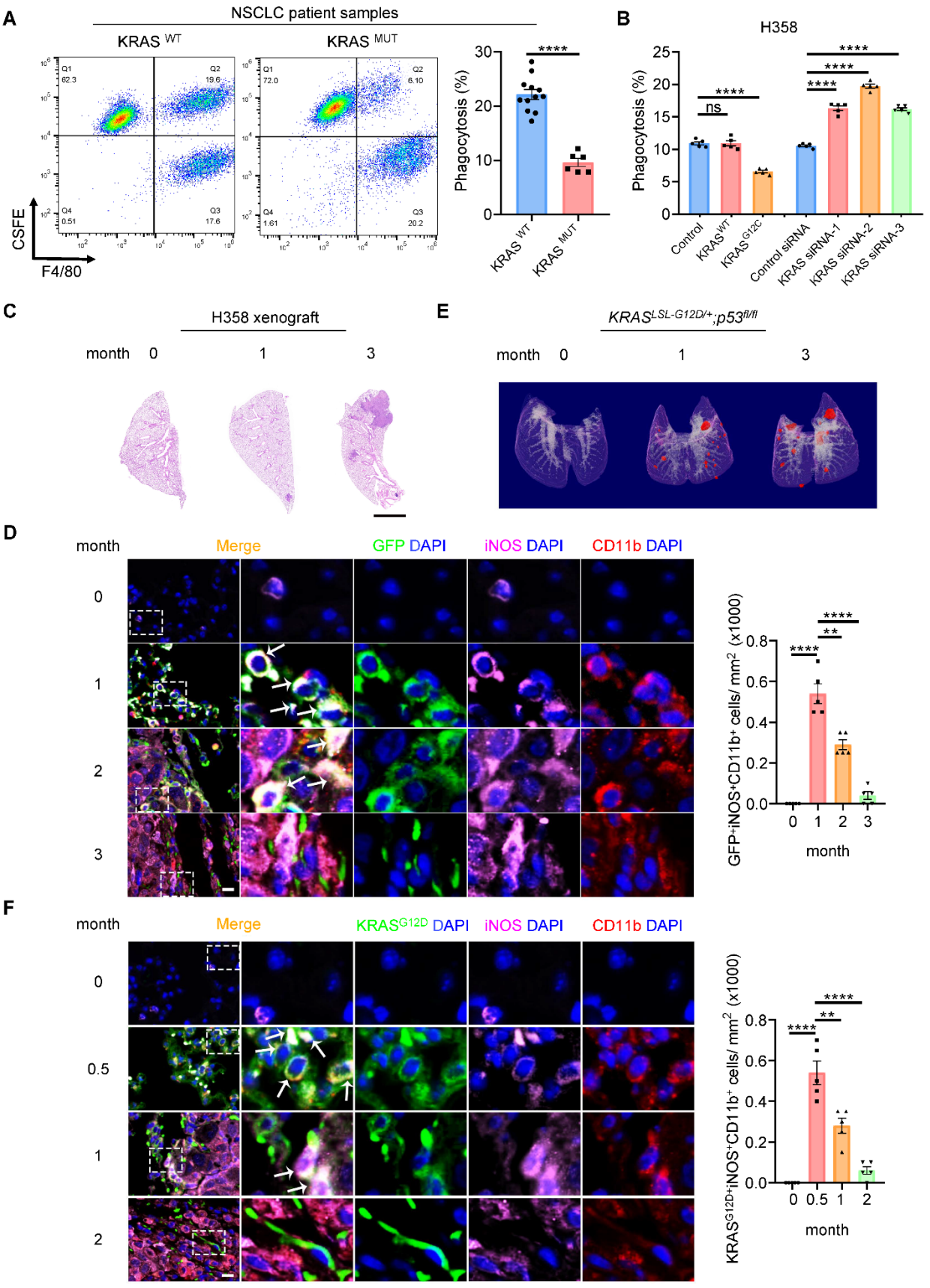
A
NSCLC patient samples
KRAS WT
KRAS MUT
CSFE
F4/80
Phagocytosis (%)
KRAS WT
KRAS MUT
B
H358
Phagocytosis (%)
Control
KRASWT
KRASG12C
Control siRNA
KRAS siRNA-1
KRAS siRNA-2
KRAS siRNA-3
C
H358 xenograft
month 0 1 3
E
KRASLSL-G12D/+;p53fl/fl
month 0 1 3
D
month
Merge
GFP DAPI
iNOS DAPI
CD11b DAPI
GFP+iNOS+CD11b+ cells/ mm2 (x1000)
month
F
month
Merge
KRASG12D DAPI
iNOS DAPI
CD11b DAPI
KRASG12D+iNOS+CD11b+ cells/ mm2 (x1000)
month

Figure 1. Oncogenic *KRAS* mutations render lung cancer cells insensitive to macrophage phagocytosis. (**A**) Tumor cells were isolated from 12 $KRAS^{WT}$ and 6 $KRAS^{MUT}$ lung adenocarcinoma patients, labeled with the fluorescent dye CFSE, incubated with human peripheral blood monocyte-derived macrophages for 2 h, stained with F4/80 and analyzed by flow cytometry. Phagocytosis rate was calculated as the percentage of $CFSE^+F4/80^+$ cells among $CFSE^+$ cells. Representative FACS results and quantification of all patients are shown. (**B**) $KRAS^{G12C}$ H358 cells were transfected with plasmids expressing $KRAS^{WT}$ or $KRAS^{G12C}$ or with three *KRAS* siRNAs. After 48 h, the cells were subjected to phagocytosis assay similar to that in **A**. Quantitative analysis (n = 5) is shown. (**C-D**) Macrophage phagocytosis of H358 cells gradually decreased with tumor progression in vivo. An animal model of lung cancer was established by tail vein injection of eGFP-labeled H358 cells into nude mice. Representative images of H&E-stained lung sections at different time points are shown in **C**. Scale bars, 2 mm. Macrophage infiltration in lung tumor tissue was assessed by CD11b (red) and iNOS (purple) staining. Representative images (Scale bars, 50 μm) and quantification results (n = 5) are shown in **D**. (**E-F**) Macrophage phagocytosis of tumor cells gradually decreased with tumor progression in genetic models of lung cancer. $Kras^{LSL\text{-}G12D/+};p53^{fl/fl}$ mice were intratracheally administered Adeno-Cre to trigger pulmonary adenocarcinoma formation. Tumor growth was monitored by micro-CT at different time points. Representative 3-D reconstructions of mouse lungs are shown in **E**. Tumors are shown in maroon. Macrophage infiltration was assessed by staining of CD11b (red), iNOS (purple) and $KRAS^{G12D}$ (green). Representative images (Scale bars, 50 μm) and quantification results (n = 5) are shown in **F**. Data are shown as mean ± SEM. **P < 0.01 and ****P < 0.0001, by unpaired t test (A) or one-way ANOVA (B, D and F).

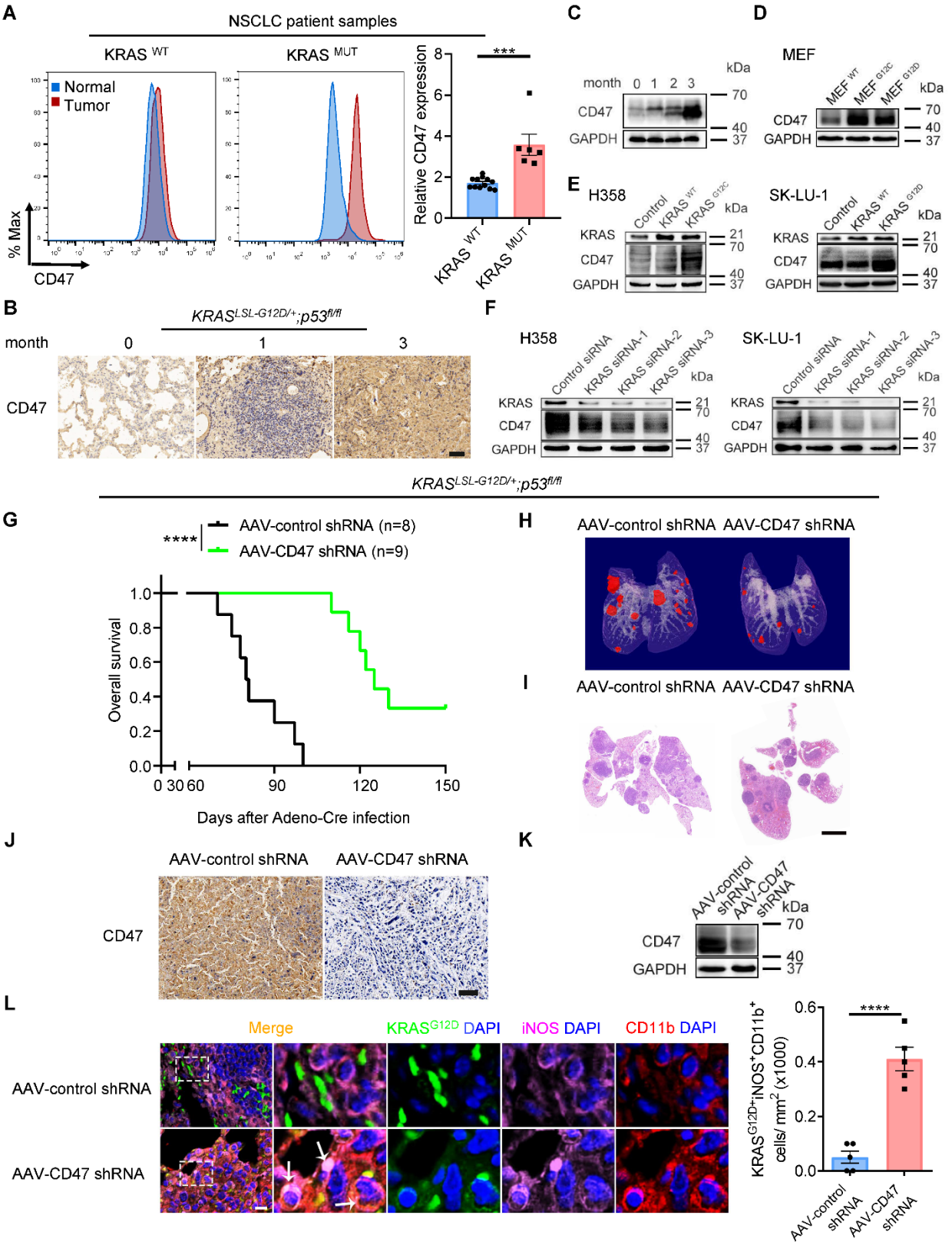
A
NSCLC patient samples
KRAS WT
KRAS MUT
Normal
Tumor
% Max
CD47
Relative CD47 expression
***
KRAS WT
KRAS MUT
B
KRASLSL-G12D/+;p53fl/fl
month
0
1
3
CD47
C
month 0 1 2 3
kDa
CD47
GAPDH
70
40
37
D
MEF
MEF WT
MEF G12C
MEF G12D
CD47
GAPDH
E
H358
SK-LU-1
Control
KRAS WT
KRAS G12C
KRAS G12D
KRAS
CD47
GAPDH
21
70
F
H358
SK-LU-1
Control siRNA
KRAS siRNA-1
KRAS siRNA-2
KRAS siRNA-3
G
****
AAV-control shRNA (n=8)
AAV-CD47 shRNA (n=9)
Overall survival
Days after Adeno-Cre infection
H
AAV-control shRNA
AAV-CD47 shRNA
I
J
CD47
K
L
Merge
KRASG12D DAPI
iNOS DAPI
CD11b DAPI
KRASG12D+iNOS+CD11b+ cells/ mm2 (x1000)

Figure 2. CD47 is required for *KRAS*-driven antiphagocytic effect in lung cancer. (**A**) Differential expression of CD47 in lung adenocarcinoma patients with different KRAS mutation status. Cancer cells were isolated from 12 $KRAS^{WT}$ and 6 $KRAS^{MUT}$ patients and analyzed for CD47 expression by FACS. Representative FACS results and quantification of all patients are shown. (**B-C**) $Kras^{LSL\text{-}G12D/+}$;$p53^{fl/fl}$ mice showed a gradual increase in CD47 expression in lung tumor tissues over time. $Kras^{LSL\text{-}G12D/+}$;$p53^{fl/fl}$ mice were sacrificed at 0, 1, 2, and 3 month, respectively, and analyzed for CD47 expression by IHC (**B**; scale bar, 20 μm) and immunoblotting (**C**). (**D**) Immunoblot analysis of CD47 expression in *Ras*-less MEFs overexpressing various KRAS mutations (WT, G12C, or G12D). (**E-F**) Effect of KRAS manipulation on CD47 expression in H358 and SK-LU-1 cells. Cells were transfected with plasmids expressing $KRAS^{WT}$ or $KRAS^{G12C}$ or $KRAS^{G12D}$ or with three *KRAS* siRNAs. After 48 h, CD47 expression was determined by immunoblotting. (**G-L**) Effect of *Cd47* knockdown on *Kras*-driven tumorigenesis and macrophage phagocytosis in vivo. The $Kras^{LSL\text{-}G12D/+}$;$p53^{fl/fl}$ mice were intratracheally administered Adeno-Cre along with an AAV encoding shRNA of *Cd47* (AAV-*Cd47* shRNA) or scrambled negative control shRNA (AAV-control shRNA). (**G**) Kaplan-Meier survival analysis. (**H**) Representative micro-CT visualization of tumors 3 months post-administration. (**I**) Representative H&E staining of lung sections. Scale bar, 2 mm. (**J**) Representative IHC staining of CD47. Scale bar, 20 μm. (**K**) Representative immunoblotting of CD47 expression in lung tumors. (**L**) Immunofluorescence staining of CD11b (red), iNOS (purple) and $KRAS^{G12D}$ (green) in lung tumors showing an increase in macrophage phagocytosis of tumor cells with *Cd47* shRNA. Representative images (scale bar, 50 μm) and quantification results (n = 5 mice) are shown. Data are shown as the mean ± SEM. ***P < 0.001 and ****P < 0.0001, by unpaired t test (A and L) or log-rank (Mantel-Cox) test (G).

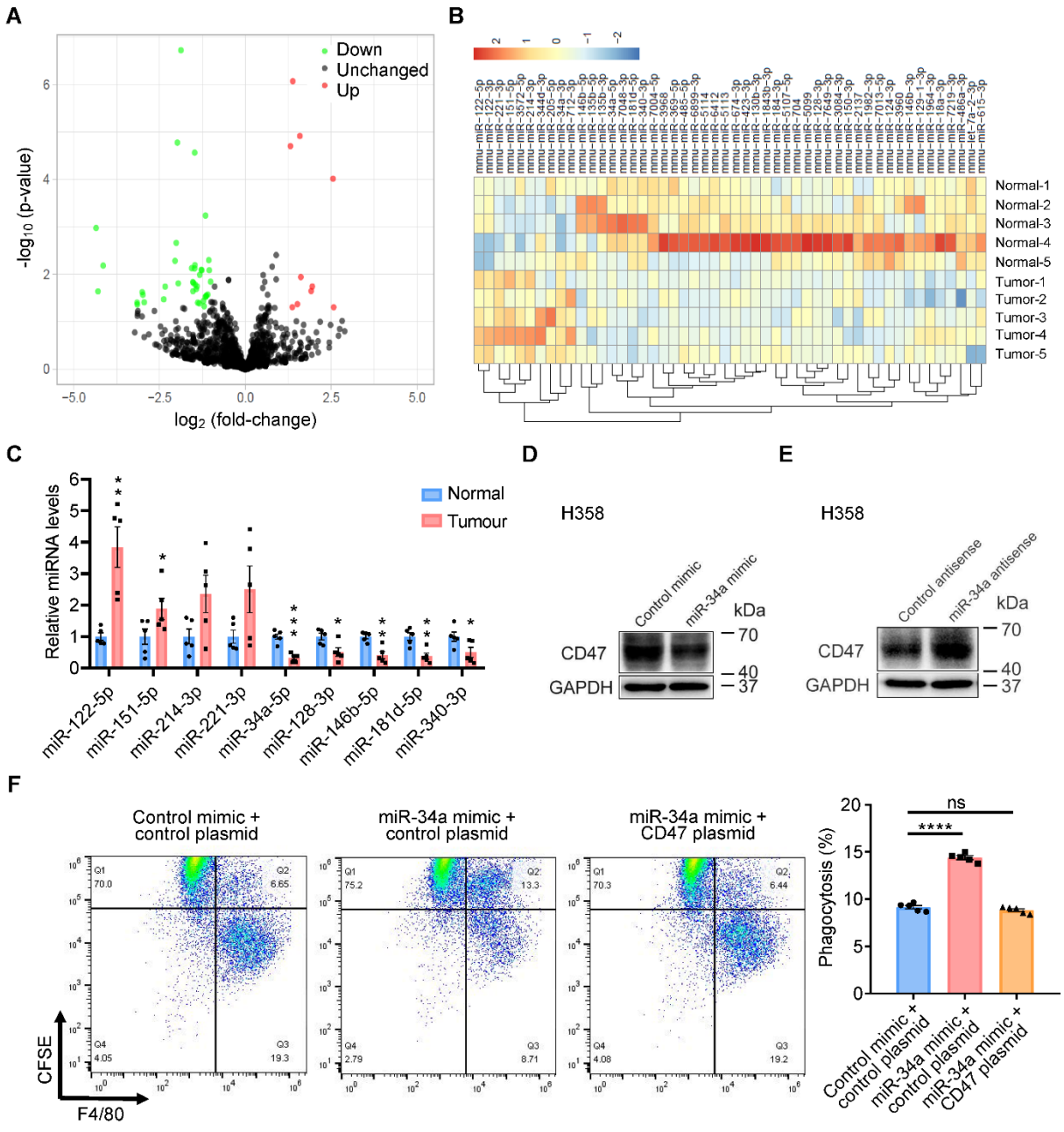

Figure 3. MiR-34a restricts CD47 activity and restores the phagocytic function of macrophages in vitro. (**A**) Scatter plot comparison illustrating miRNAs that were differentially expressed between malignant and normal lung tissues of the *Kras*$^{LSL\text{-}G12D/+}$ mice. (**B**) Dendrogram generated by unsupervised hierarchical cluster analysis showing the separation of tumors from the normal tissues based on miRNA profiling (10 upregulated *vs.* 40

downregulated). (**C**) Quantitative RT-PCR analysis of the 9 most changed miRNAs in **A** (n = 5 mice). (**D**-**E**) Effect of miR-34a mimic or miR-34a antisense on CD47 expression in H358 cells. (**F**) Effect of miR-34a mimic on macrophage phagocytosis of H358 cells. Cells were transfected with miR-34a mimic and/or CD47-expressing plasmid. After 48 h, cells were subjected to macrophage phagocytosis assay. Representative FACS images and quantification results (n = 5) are shown. Data are shown as mean ± SEM. *P < 0.05, **P < 0.01, ***P < 0.001 and ****P < 0.0001, by unpaired t test (C) or one-way ANOVA (F).

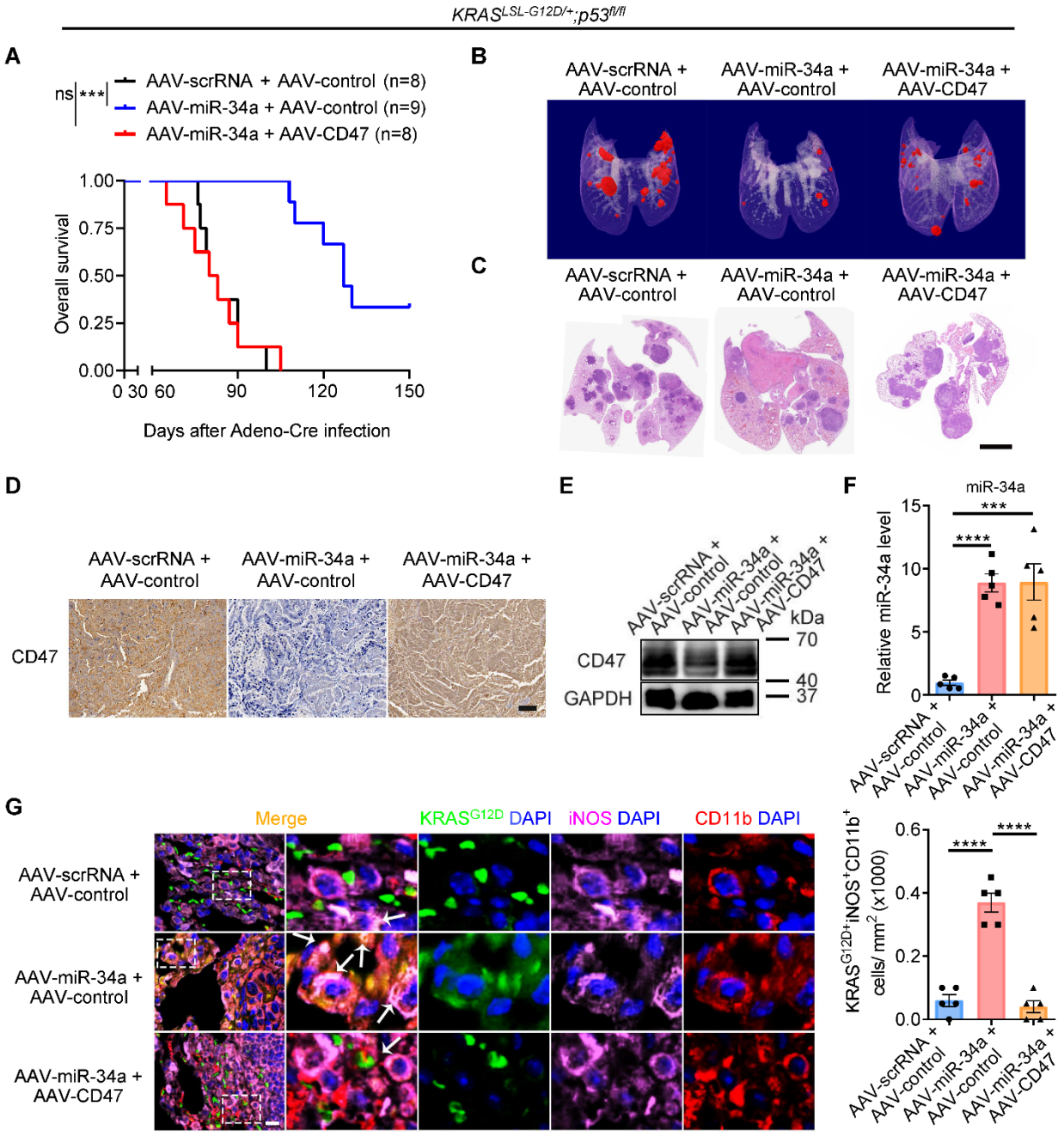

Figure 4. MiR-34a inhibits *Kras*-driven tumorigenesis and promotes macrophage infiltration in vivo. The *Kras*$^{LSL\text{-}G12D/+}$;*p53*$^{fl/fl}$ mice were intratracheally administered Adeno-Cre along with AAV-miR-34a (or control AAV-scrRNA) and AAV-*CD47* (or AAV-control). (**A**) Kaplan-Meier survival analysis. (**B**) Representative micro-CT visualization of tumors 3 months post-administration. (**C**) Representative H&E staining of lung sections. Scale bar, 2 mm. (**D**)

Representative IHC staining of CD47 in lung sections. Scale bar, 20 μm. (**E**) Representative immunoblotting of CD47 in lung tumors. (**F**) miR-34a levels in lung tumors (n = 5). (**G**) Immunofluorescence staining of CD11b (red), iNOS (purple), $KRAS^{G12D}$ (green) and DAPI (blue) in lung tumors showing an increase in macrophage phagocytosis of tumor cells with AAV-miR-34a which was rescued by AAV-CD47. Representative images (Scale bar, 50 μm) and quantification results (n = 5 mice) were shown. Data are shown as mean ± SEM. ***P < 0.001 and ****P < 0.0001, by one-way ANOVA (F and G) or log-rank (Mantel-Cox) test (A).

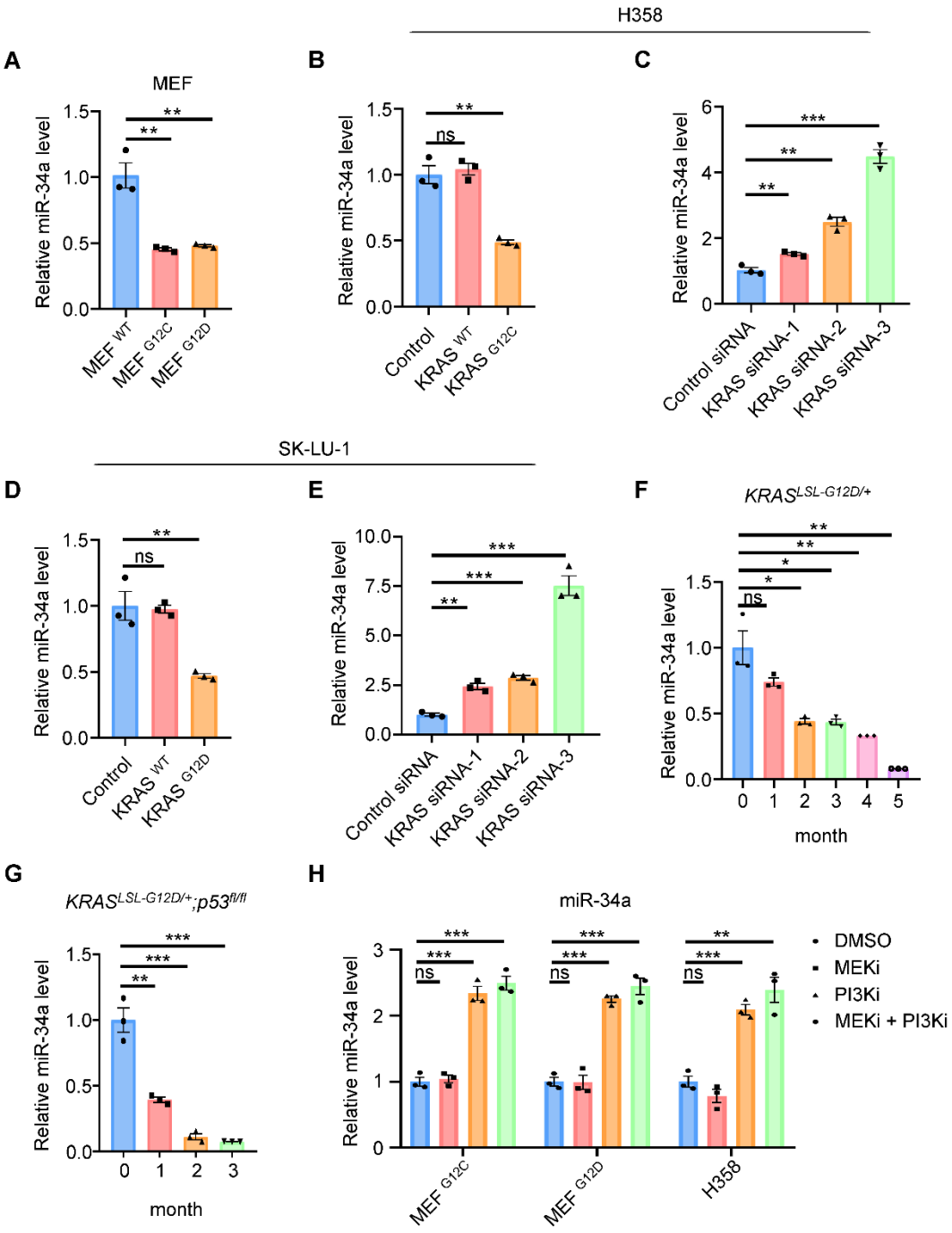

Figure 5. KRAS signaling modulates miR-34a expression in lung cancer cell lines and animal models. (**A-E**) Quantitative RT-PCR analysis of the effect of *Kras* mutation status on the miR-34a expression levels in MEFs (**A**); H358 cells overexpressing $KRAS^{WT}$ or $KRAS^{G12C}$ (**B**); H358 cells transfected with three *KRAS* siRNAs (**C**); SK-LU-1 cells overexpressing $KRAS^{WT}$ or

KRAS^{G12D} (**D**); or SK-LU-1 cells transfected with three *KRAS* siRNAs (**E**) (n = 3). (**F-G**) Quantitative RT-PCR analysis of the relative expression levels of miR-34a in the whole lung extracts from *Kras*$^{LSL\text{-}G12D/+}$ or *Kras*$^{LSL\text{-}G12D/+}$*;p53*$^{fl/fl}$ mice at different time points (n = 3 mice). (**H**) Effect of MEK and PI3K inhibition on the expression of miR-34a. MEF^{G12C}, MEF^{G12C}, or H358 cells was treated with DMSO, MEK inhibitor, PI3K inhibitor or a combination of both inhibitors. The relative miR-34a expression levels were determined by quantitative RT-PCR (n = 3). Data are shown as mean ± SEM. *P < 0.05, **P < 0.01 and ***P < 0.001, by one-way ANOVA (A-H).

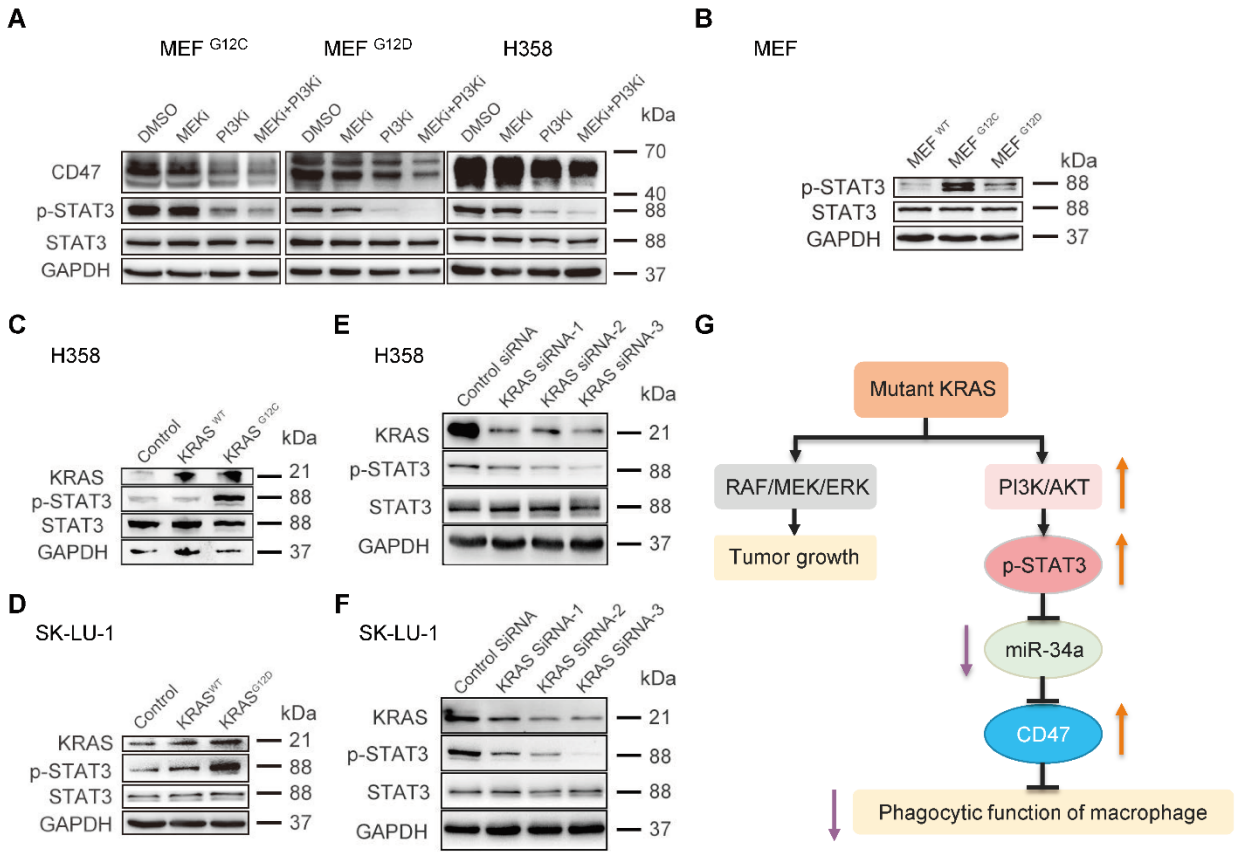

Figure 6. KRAS modulates CD47 expression through the PI3K-STAT3-miR-34a signaling axis. (**A**) Effect of MEK and PI3K inhibition on the expression of CD47, p-STAT3 and total STAT3 in MEFs and H358 cells. (**B-F**) Western blot analysis of the expression levels of KRAS, p-STAT3 and total STAT3 in MEFs (**B**); H358 cells overexpressing $KRAS^{WT}$ or $KRAS^{G12C}$ (**C**); SK-LU-1 cells overexpressing $KRAS^{WT}$ or $KRAS^{G12D}$ (**D**); H358 cells transfected with three *KRAS* siRNAs (**E**); or SK-LU-1 cells transfected with three *KRAS* siRNAs (**F**). (**G**) Schematic of the signaling pathways involved in the regulation of CD47 expression and macrophage phagocytic function by *KRAS* mutation.

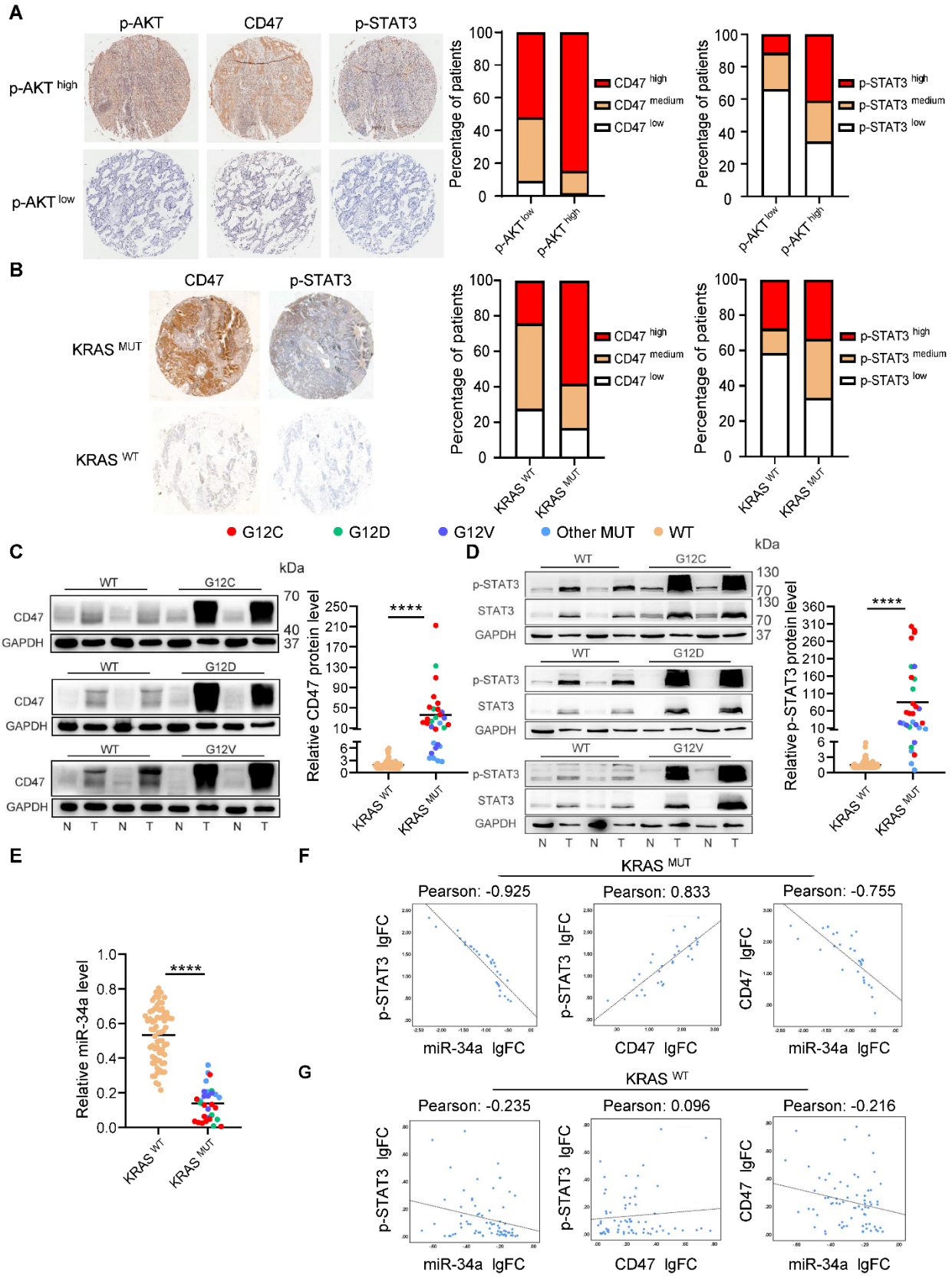
A
p-AKT
CD47
p-STAT3
p-AKT high
p-AKT low
Percentage of patients
CD47 high
CD47 medium
CD47 low
p-STAT3 high
p-STAT3 medium
p-STAT3 low
B
KRAS MUT
KRAS WT
G12C
G12D
G12V
Other MUT
WT
C
kDa
GAPDH
Relative CD47 protein level
****
D
STAT3
Relative p-STAT3 protein level
E
Relative miR-34a level
F
KRAS MUT
Pearson: -0.925
Pearson: 0.833
Pearson: -0.755
p-STAT3 lgFC
CD47 lgFC
miR-34a lgFC
G
KRAS WT
Pearson: -0.235
Pearson: 0.096
Pearson: -0.216

Figure 7. Clinical relevance of *KRAS* mutation status and CD47 expression in lung adenocarcinoma patients. (**A**) Correlation analysis of KRAS activity and CD47 expression in the first patient cohort containing 157 lung adenocarcinoma samples. IHC staining was performed to analyze CD47 and p-STAT3 in the tissue microarray chips stratified by high or low KRAS activity (measured by p-AKT levels due to the lack of *KRAS* mutation information). Left: representative IHC images. Right: bar graph showing the expression of CD47 and p-STAT3 in the low and high p-AKT patients (n = 98 and 59, respectively). CD47 and p-STAT3 expression status were stratified based on IHC scores. (**B**) IHC analysis of CD47 and p-STAT3 in a homemade tissue microarray containing 40 lung adenocarcinoma samples (28 $KRAS^{WT}$ and 12 $KRAS^{MUT}$). Left: representative IHC images. Right: bar graph showing the expression of CD47 and p-STAT3 in $KRAS^{WT}$ and $KRAS^{MUT}$ tumors (n = 28 and 12, respectively). The CD47 and p-STAT3 expression status were stratified based on IHC scores. (**C**-**E**) Correlation analysis of *KRAS* mutation status and the expression of CD47, p-STAT3 and miR-34a in the third lung adenocarcinoma patient cohort with *KRAS* mutation status determined by deep sequencing. (**C**) Immunoblotting analysis of CD47 expression in $KRAS^{WT}$, $KRAS^{G12C}$, $KRAS^{G12D}$ or $KRAS^{G12V}$ patients. Left: representative blots (N: normal; T: tumor). Right: quantitative analysis (n = 70 $KRAS^{WT}$ and 30 $KRAS^{MUT}$, respectively). (**D**) Immunoblotting analysis of p-STAT3 expression in $KRAS^{WT}$ and $KRAS^{MUT}$ patients. (**E**) Quantitative RT-PCR analysis of miR-34a levels in $KRAS^{WT}$ and $KRAS^{MUT}$ patients. (**F**-**G**) Pearson's correlation coefficient analysis of the correlations among p-STAT3, miR-34a and CD47 in the $KRAS^{MUT}$ (**F**) and $KRAS^{WT}$ (**G**) lung adenocarcinoma samples. FC, fold change. Data are shown as mean ± SEM. ****P < 0.0001, by unpaired t test (C, D and E) or Pearson correlation test (F and G).

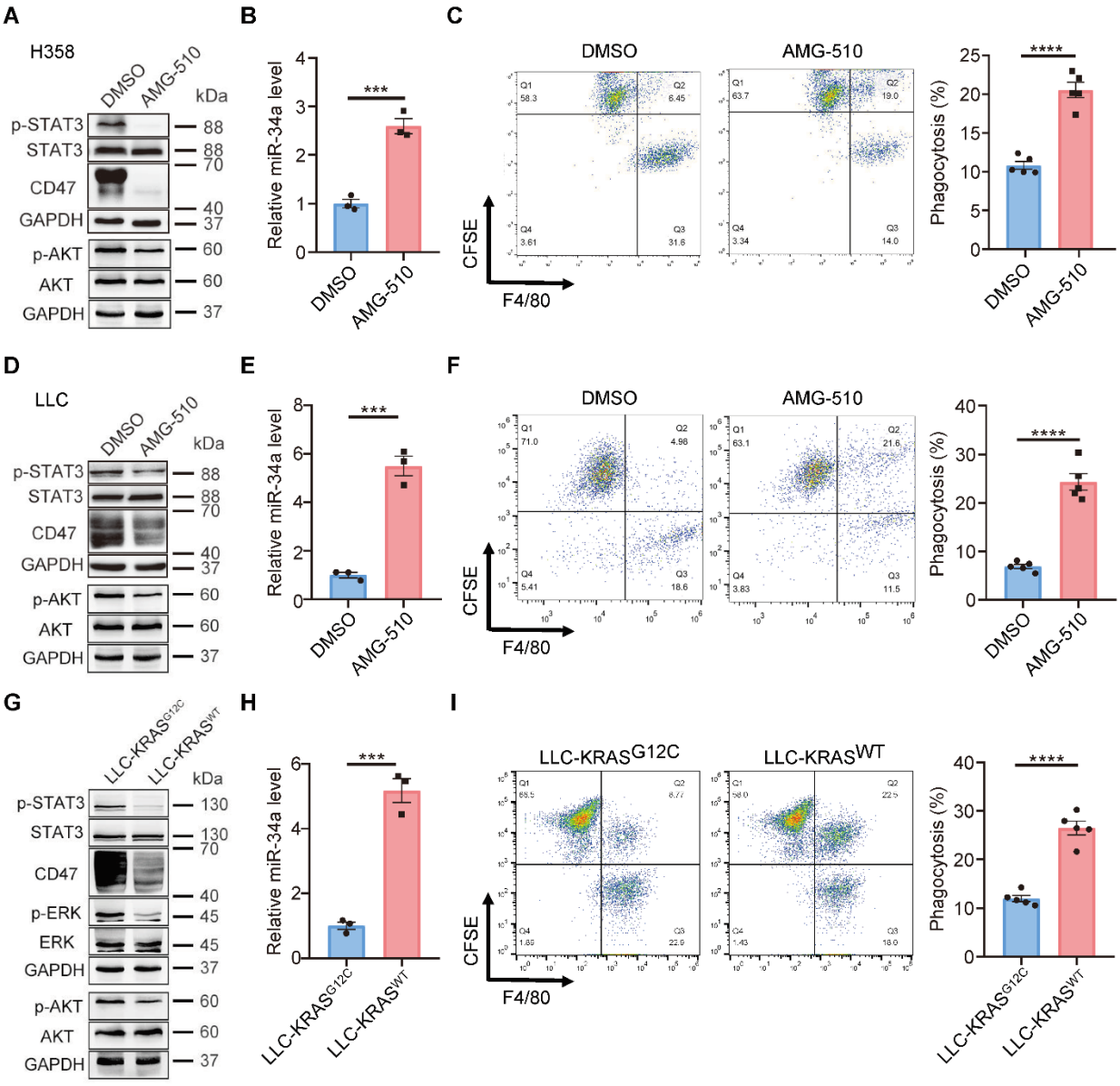

Figure 8. The KRAS^{G12C} inhibitor AMG 510 inhibits CD47 signaling and promotes macrophage phagocytosis of tumor cells in vitro. (**A-C**) AMG 510 treatment renders H358 cells sensitive to phagocytosis by macrophages. (**A-B**) Effect of AMG 510 treatment (24 h) on the expression levels of p-STAT3, p-AKT, CD47 and miR-34a in H358 cells. **(C)** KRAS^{G12C} inhibition increased phagocytosis of H358 cells by macrophages. Cells were treated with AMG 510 for 24 h before coculture with human peripheral blood monocyte-derived macrophages. Phagocytosis of H358 cells by macrophages was analyzed by flow cytometry. Representative

FACS plots and quantification (n = 5) are shown. (**D-F**) AMG 510 treatment renders LLC cells sensitive to phagocytosis by macrophages. Experiments identical to that in **A-C** were carried out. (**G-I**) Effect of *Kras* mutation status on CD47 expression and macrophage phagocytosis in LLC cells. LLC cells (heterozygous for $Kras^{G12C}$) were converted to $Kras^{WT}$ using CRISPR/Cas9. Experiments similar to that in **A-C** were then carried out for the cell pair. Data are shown as mean ± SEM. ***P < 0.001 and ****P < 0.0001, by unpaired t test (B, C, E, F, H and I).

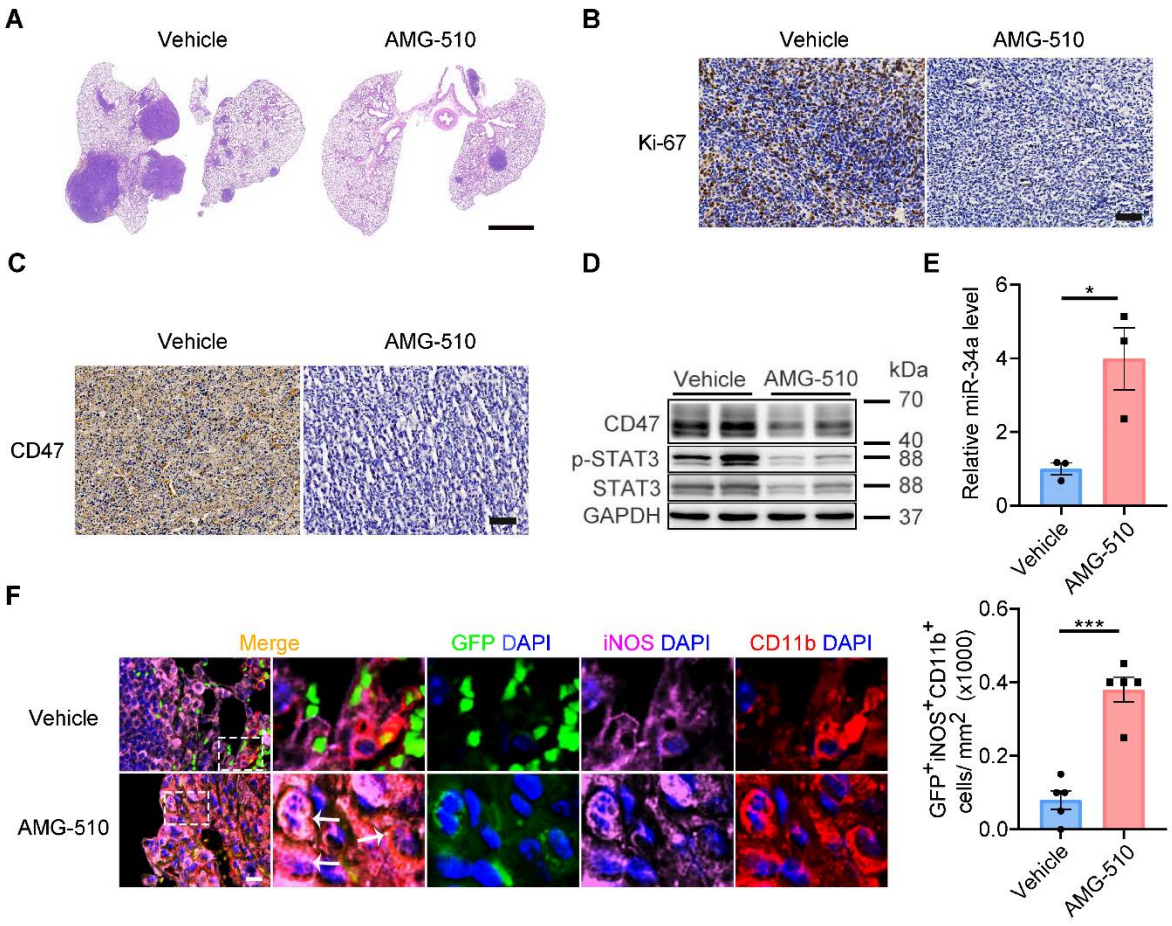

Figure 9. The KRAS^{G12C} inhibitor AMG 510 inhibits CD47 signaling and promotes macrophage phagocytosis of tumor cells in vivo. eGFP-labeled LLC cells were injected via tail vein into C57BL/6 mice. After tumor formation, mice were administered AMG 510 via oral gavage for 8 days. (**A**) Representative H&E-stained lung sections. Scale bar, 2 mm. (**B**) Representative Ki-67 staining of lung sections. Scale bar, 20 μm. (**C**) Representative CD47 staining of lung sections. Scale bar, 20 μm. (**D**) Representative immunoblots of CD47 and p-STAT3 in lung tumors. (**E**) Quantitative RT-PCR analysis of miR-34a expression in lung tumors (n = 3). (**F**) Immunofluorescence staining of CD11b (red), iNOS (purple) and DAPI (blue) in lung tumors showing an increase in macrophage phagocytosis of tumor cells with AMG 510 treatment. Representative images (scale bar, 50 μm) and quantification results (n = 5 mice) are

shown. Data are shown as mean ± SEM. *P < 0.05 and ***P < 0.001, by unpaired t test (E and F).